PHYSICAL REVIEW B **81**, 064404 (2010)

Itinerant half-metallic ferromagnets Co_2TiZ (Z=Si, Ge, Sn): *Ab initio* calculations and measurement of the electronic structure and transport properties

Joachim Barth, Gerhard H. Fecher, Benjamin Balke, Siham Ouardi, Tanja Graf, and Claudia Felser*
Institut für Anorganische und Analytische Chemie, Johannes Gutenberg Universität, D-55099 Mainz, Germany

Andrey Shkabko and Anke Weidenkaff
EMPA, Swiss Federal Laboratories for Materials Testing and Research, Solid State Chemistry and Catalysis, CH-8600 Duebendorf, Switzerland

Peter Klaer and Hans J. Elmers
Institut für Physik, Johannes Gutenberg Universität, D-55099 Mainz, Germany

Hideki Yoshikawa, Shigenori Ueda, and Keisuke Kobayashi
NIMS Beamline Station at SPring-8, National Institute for Materials Science, Hyogo 679-5148, Japan

(Received 11 September 2009; revised manuscript received 7 December 2009; published 5 February 2010)

This work reports on *ab initio* calculations and experiments on the half-metallic ferromagnetic Heusler compounds Co_2TiZ (Z=Si, Ge, Sn). Aim is a comprehensive study of the electronic-structure and thermoelectric properties. The impact of the variation in the main group element Z on those properties is discussed. X-ray diffraction was performed on the compounds and the lattice parameters are compared to other Co_2-based compounds. Hard x-ray photoemission measurements were carried out and the results are compared to the calculated electronic structure. The experimentally determined electronic structure, magnetic properties, and transport measurements agree well with the calculations. The electronic and thermoelectric properties were measured for temperatures from 2 to 950 K. The electrical resistivity exhibits a pronounced *cusp*-type anomaly at the Curie temperature (T_C) where a distinct maximum appears. The strongest magnetic-scattering resistivity is found in Co_2TiSn with 1.7 $\mu\Omega$ m. The resistivity becomes nearly constant at higher temperatures. The measured thermal conductivity is on the order of 5 W m^{-1} K^{-1}. The measured Seebeck coefficient $[S(T)]$ is similar in all three compounds and exhibits also a very distinct anomaly at the magnetic phase transition. A maximum value of -50 μV K^{-1} is found for Co_2TiSn at T_C. Most interesting is that S stays constant above the Curie temperature in all three compounds.

DOI: 10.1103/PhysRevB.81.064404 PACS number(s): 72.15.Jf, 61.05.cp, 71.15.Mb, 71.20.Be

I. INTRODUCTION

Heusler compounds have the general composition X_2YZ, where X and Y are transition metals and Z is a main group element. An exceptional electronic structure was found in the Heusler compounds Co_2MnAl and Co_2MnSn by Kübler, Williams, and Sommers[1] who proposed that the minority-spin density at the Fermi energy vanishes in those compounds. This prediction was later extended to include also other Heusler compounds[2–4] and specially all compounds based on Co_2.[5] All those compounds are supposed to exhibit a complete spin polarization at the Fermi energy such that they behave as a metal for one spin direction and as an insulator for the other one. Compounds with that special behavior are called half-metallic ferromagnets.[6] It was concluded that half-metallic ferromagnetism should lead to peculiar transport properties. In this paper, the transport properties of Heusler compounds containing Co and Ti are investigated with respect to their use as materials for magnetic or thermoelectric devices. The interesting feature of these compounds is that they do not carry a strongly localized magnetic moment at the atom in the Y position as is observed if Y is Mn.

The research in the field of thermoelectric materials has experienced a great increase in the recent years due to their practical application as power generators or as cooling and heating devices. Several material classes, such as Clathrates,[7] Bismuth Tellurides,[8] Skutterudites,[9,10] and Heusler compounds with $C1_b$ structure[11] have been investigated lately. Only few investigations have been carried out for Heusler compounds with $L2_1$ structure. The investigations were mainly based on the compound Fe_2VAl.[12,13] New ways of so-called *spincalorics* try to combine magnetic and thermoelectric properties in a single device that allows to manipulate spin-transport phenomena.

This paper focuses on the material class Co_2TiZ, (Z=Si, Ge, or Sn) with $L2_1$ structure. The Heusler compounds are attractive as materials combining magnetic and thermoelectric properties due to their peculiar electronic structure and its easy tunability. The physical properties can be easily changed by the substitution of atoms with ones that have similar radii and charges. Likewise the magnetic moments, resistivity or the Seebeck coefficient can be manipulated that way. This is especially important for new types of magneto-thermoelectric devices because a tuning of the carrier concentration allows to optimize the efficiency of the materials.

The efficiency of a purely thermoelectric material is described by the figure of merit (ZT) (Ref. 14) that depends on the temperature T as well as the electronic- and thermal-transport properties. State of the art materials are filled scutterudite compounds with a $ZT \approx 1.2$ at 700 K,[9,10] semiconducting clathrates with a $ZT \approx 1$ at 700 K,[7] and Heusler compounds with $C1_b$ structure with a $ZT \approx 1.5$ at 800 K.[11] Indeed, such materials naturally do not carry magnetic properties. Therefore, new materials have to be found that are optimized for thermoelectric as well as magnetic properties.

In this paper, the properties of the Heusler compounds Co_2TiZ (Z=Si, Ge, Sn) are investigated theoretically and experimentally. Since the compounds are supposed to be half-metallic ferromagnets all calculations are carried out for spin-polarized and non-spin-polarized ground states. The results are compared to the experimental data and discussed in the respective chapters. X-ray diffraction was performed for the structure determination and the obtained cell parameters were set into context of other compounds with similar compositions. For the surface investigations energy-dispersive x-ray spectroscopy (EDX) was used to ensure the homogeneity of the samples. The magnetic properties as well as the obligatory transport measurements were performed. In a final characterization step, hard x-ray photoelectron spectroscopy (HAXPES) was performed on the compounds to experimentally determine the electronic structure and compare it to the calculated results.

II. COMPUTATIONAL DETAILS

The electronic structure of the compounds was calculated by means of the full-potential linearized augmented plane-wave (FLAPW) method as implemented in WIEN2K.[15,16] The exchange-correlation functional was taken within the generalized gradient approximation (GGA).[17] A $25 \times 25 \times 25$-point mesh was used as base for the integration in the cubic systems resulting in 455 k points in the irreducible wedge of the Brillouin zone. The energy convergence criterion was set to 10^{-5} Ry and simultaneously the criterion for charge convergence to $10^{-3}e^-$. The muffin-tin radii were set to $2.5a_{0B}$ (a_{0B}=0.5291772 Å) for the transition metals as well as the main group element. Further details of the calculations are reported in Ref. 5.

A. Electron transport

BOLTZTRAP (Ref. 18) was used for the calculation of the transport properties. This program is based on Boltzmann transport theory. In the present work it was modified to allow a simultaneous treatment of the two spin channels and the resulting spin-averaged transport quantities. The changes were necessary, in particular, because one of the spin channels is supposed to be semiconducting in the investigated materials while the other is metallic. For the calculation of transport properties, an enlarged 40^3 mesh with 1661 irreducible points was used with WIEN2K. The final calculations with BOLTZTRAP were performed on an eightfold larger k grid using the tetrahedron method and energy steps of $\Delta E/k_B = 5/80$ K.

The basics of transport theory are described in the textbooks of Ziman[19] or Mizutani.[20] In general, the Boltzmann transport equations allow to calculate the electrical conductivity from the electronic structure.[18,20,21] Neglecting effects of an external magnetic field as well as higher-order terms in the electric field ∇V (where V is the electric potential) and temperature gradient ∇T, the linear transport equations for the electric (J_i) and thermal (U_i) current densities are given by

$$J_i = \sigma_{ij}\nabla_j V + \nu_{ij}\nabla_j T,$$

$$U_i = -T\nu_{ij}\nabla_j V + \kappa_{ij}\nabla_j T, \tag{1}$$

where i,j assign the directions in space. σ_{ij}, ν_{ij}, and κ_{ij} are the electric- and thermal-conductivity tensors. σ_{ij} and κ_{ij} are related through the Lorentz number L by $\kappa_{ij} = -LT\sigma_{ij}$. The conductivity tensors depend on the electronic structure, that is on the $E(k)$ relation. In particular, they depend on the group velocities $\upsilon_\alpha(k)$ that are given by the derivatives of the band dispersion $\upsilon_\alpha(k) = \frac{1}{\hbar}\frac{\partial E_k}{\partial k_\alpha}$. In relaxation time approximation one finds the general transport tensor ϵ_{ij} from

$$\tau_{n,k}\epsilon_{ij}(k) = e^2 \upsilon_i(n,k)\upsilon_j(n,k),$$

$$\epsilon_{ij}(E) = \int \epsilon_{ij}(k)\frac{dS}{\nabla_k E(k)}, \tag{2}$$

where n is the band index, e is the electron charge, and $\tau_{n,k}$ is the relaxation time. Further, it is noted that the density of states is defined by

$$n(E)dE = \frac{1}{4\pi^3}\int\int \frac{dS}{\nabla_k E(k)}dE. \tag{3}$$

With help of relaxation-time approximation and transport tensor ϵ_{ij}, the electric conductivity tensor is given by

$$\sigma_{ij} = -e^2\int_0^\infty \tau_k \epsilon_{i,j}(E)\frac{\partial f(E,\mu,T)}{\partial E}dE, \tag{4}$$

where μ is the chemical potential and $f(E,\mu,T)$ is the Fermi-Dirac distribution. In metals, the chemical potential μ corresponds to the ground-state Fermi energy ϵ_F in a good approximation [note: $\mu(T=0) = \epsilon_F$].

The tensors σ_{ij}, ν_{ij}, and κ_{ij} are diagonal in orthorhombic systems and the diagonal elements are all equal in cubic or isotropic systems (for a proof see Ref. 21). This means that in isotropic systems, likewise cubic crystals, only the diagonal terms $\sigma_{ii} = \sigma$ exist. In analogy, the other tensors will also become scalar in isotropic systems.

The relaxation time $\tau = \tau_k$ depends on the electron momentum k, in general. However, detailed studies of the k dependence of τ have shown that it is not dependent on the k direction to a good approximation.[22] Although assumed to be independent of k, the relaxation time $\tau = \tau(T)$ may be temperature dependent for certain scattering processes of the electrons. In general, τ is expressed as

$$\frac{1}{\tau_p} = \frac{1}{\tau_{e\text{-}e}} + \frac{1}{\tau_{e\text{-}imp}} + \frac{1}{\tau_{e\text{-}ph}} + \cdots. \tag{5}$$

Here the index p is used to assign a paramagnetic (PM) or diamagnetic material. For electron-electron scattering ($\tau_{e\text{-}e}$) and for scattering of electrons at impurities ($\tau_{e\text{-}imp}$) the temperature dependence is negligible. The relaxation time for electron-phonon scattering ($\tau_{e\text{-}ph}$) depends on the thermal excitation of phonons and thus on the temperature, too. In magnetic materials additional terms may appear,

$$\frac{1}{\tau_m} = \frac{1}{\tau_{e\text{-}mag}} + \frac{1}{\tau_{sd}} + \dots, \tag{6}$$

such that the overall relaxation time is given by $1/\tau = 1/\tau_p + 1/\tau_m$. $\tau_{e\text{-}mag}$ arises from electron-magnon scattering. This relaxation time is temperature dependent because it depends on the thermal occupation of the magnons and therefore on the Curie temperature. Finally, τ_{sd} describes the so-called spin-disorder scattering.

In the following, the k or E dependence of the relaxation time τ is neglected and cubic crystal systems are assumed. This allows to remove τ from the integral and to drop the directional indices. The result for the conductivity is

$$\frac{\sigma}{\tau} = -e^2 \int_0^\infty \epsilon(E) \frac{\partial f(E,\mu,T)}{\partial E} dE. \tag{7}$$

Similar to the electric conductivity, the thermal-transport properties are calculated from the *ab initio* electronic structure making use of the Boltzmann transport equations.[18,20,21] The electronic part of the thermal conductivity is found from the integral,

$$\frac{\kappa^0}{\tau} = -\frac{1}{T} \int_0^\infty \epsilon(E)(E-\mu)^2 \frac{\partial f(E,\mu,T)}{\partial E} dE. \tag{8}$$

In general, the Seebeck coefficient is also a tensor and derived from the electrical- and thermal-conductivity tensors,

$$S_{ij} = [\sigma_{ij}]^{-1} \nu_{ij}. \tag{9}$$

Similar to the electric-conductivity integral [Eq. (7)], the nominator for cubic systems is simplified to

$$\frac{\nu}{\tau} = -\frac{e}{T} \int_0^\infty \epsilon(E)(E-\mu) \frac{\partial f(E,\mu,T)}{\partial E} dE \tag{10}$$

and the result for the Seebeck coefficient is $S = \nu/\sigma$. The thermal- and electric-conductivity integrals contain the relaxation time τ, which is identical in both cases. S does therefore not dependent on the relaxation time if assuming that τ is independent of the electron momentum k,

$$S = -\frac{1}{eT} \frac{\int_0^\infty \epsilon(E)(E-\mu) \frac{\partial f(E,\mu,T)}{\partial E} dE}{\int_0^\infty \epsilon(E) \frac{\partial f(E,\mu,T)}{\partial E} dE}. \tag{11}$$

Along with the Seebeck coefficient, the electronic thermal conductivity at zero electric current is defined in an isotropic system by $\kappa^e = \kappa^0 - T\nu S$. S, as defined by Eq. (9), is small in the materials investigated here and κ^e is dominated by κ^0 wherefore the second term will be omitted in the following.

For the reason of charge neutrality, the number of thermally created holes (h^+) below ϵ_F has to be identical with the number of thermally excited electrons (e^-) above ϵ_F. This leads to a shift of the chemical potential at finite temperature whenever the density of states is not constant in the vicinity of the Fermi energy. The temperature dependence of the chemical potential $\mu(T)$ of a metal is approximately given by

$$\mu(T) \approx \epsilon_F - \frac{\pi^2}{6}(k_B T)^2 \left[\frac{\frac{dn(E)}{dE}}{n(E)} \right]_{E=\epsilon_F}. \tag{12}$$

The chemical potential obviously shifts to lower energies if the density of states at the Fermi energy increases $[dn(E)/dE > 0]$ and to higher energies if $n(E)$ decreases at ϵ_F. In metals, however, this shift is usually small and cannot exceed the width of $df(E)/dE$ that is on the order of few tens of millielectron volts at moderate temperatures.

B. Phonons

The vibrational properties of the investigated compounds were calculated by means of PHONON (Ref. 23) on the base of the results from WIEN2K. The primitive cell containing four atoms was enlarged to a cell with 16 distinguished atoms to calculate the Hellmann-Feynman forces for the phonon analysis. For these calculations, a force convergence criterion of 10^{-4} Rya_{0B}^{-1} was used in addition to the energy convergence criterion.

The knowledge about the phonon-dispersion $\omega(q)$ relation and the accompanied density of states $g(\omega)$ allows to calculate various physical properties related to lattice vibrations. Most basically, the temperature dependence of the lattice heat capacity of the whole crystal is described in the harmonic approximation by[24]

$$C_L = r k_B \int \left(\frac{\hbar\omega}{k_B T}\right)^2 \frac{\exp\left(\frac{\hbar\omega}{k_B T}\right)}{\left[\exp\left(\frac{\hbar\omega}{k_B T}\right) - 1\right]^2} g(\omega) d\omega, \tag{13}$$

where r is the number of degrees of freedom, k_B is the Boltzmann constant, and h is the Planck constant. Most often, the properties depending on the lattice vibrations are described by models based on the Debye temperature Θ_D. Once knowing $g(\omega)$, Θ_D is found from a fit of C_L [Eq. (13)] to the Debye model with $g_D(\omega) \propto \omega^2$. This procedure results in a temperature-dependent $\Theta(T)$ and approaches the classical value for $T > \Theta_D$. It is worthwhile to note that the same procedure can be used to find experimental values of Θ_D from the measured heat capacity.

The heat transport by lattice vibrations plays an important role for the thermoelectric-transport properties, besides the electronic heat conductivity that was given by Eq. (8). Within the quasiharmonic approximation and with the aid of the Debye model, the phonon thermal conductivity is expressed in the following form:

$$\kappa_L(T) = \frac{k_B}{2\pi^2 v_s} \left(\frac{k_B T}{\hbar}\right)^3 \int_0^{\Theta_D/T} \tau_L \frac{x^4 e^x}{(e^x - 1)^2} dx. \tag{14}$$

Here κ_L is the phonon thermal conductivity, $x = \hbar\omega/(k_B T)$ is a dimensionless quantity, ω is the phonon frequency, Θ_D is the Debye temperature, v_s is the velocity of sound, and τ_L is the total phonon-scattering relaxation time. In general, it is temperature and frequency dependent and cannot be eliminated as easy from the integral as the τ in the electronic-transport coefficients.

Similar to the relaxation time entering the electronic-transport properties, τ_L consists also of several parts arising from different scattering processes. The following processes are assumed to limit the heat conduction mediated by phonons: scattering at grain boundaries, umklapp scattering, electron-phonon scattering, and Rayleigh-type point-defect scattering. The phonon-scattering relaxation rate is then written as

$$\frac{1}{\tau_L} = \frac{1}{\tau_b} + \frac{1}{\tau_u} + \frac{1}{\tau_p} + \frac{1}{\tau_{e\text{-}ph}} = c_b + c_u\omega^2 T^3 e^{-\Theta_D/T} + c_p\omega^4 + c_{e\text{-}ph}\omega^2. \tag{15}$$

Here c_b, c_u, c_p, and $c_{e\text{-}ph}$ are the parameters which are related to the strength of boundary, umklapp, point-defect scattering, and electron-phonon interaction, respectively. Boundary scattering gives temperature- and frequency-independent relaxation times $(\tau_b \approx v_s/D, D := \text{grain diameter})$ and results in a T^3-type dependence of κ_L on T at low temperatures. Rayleigh-type scattering will strongly suppress high-frequency phonons since the relaxation time τ_p is proportional to ω^{-4}. In case of localized impurities, an additional resonant scattering term

$$\frac{1}{\tau_i} = \frac{c_i\omega^2 T^2}{(\omega_E^2 - \omega^2)^2 + \gamma\omega_E^2\omega^2} \tag{16}$$

appears that describes the concentration of impurities causing resonant scattering. γ is the average deformation potential. The resonant vibration frequency ω_E is determined by $k_B\Theta_E/\hbar$, where Θ_E is the Einstein temperature of the localized vibrational mode.

As mentioned in Sec. I, the efficiency of a thermoelectric material is characterized by the *figure of merit* that is defined by[14]

$$ZT = \frac{S^2 \cdot \sigma}{\kappa} T = \frac{S^2 T}{\kappa \cdot \rho} \tag{17}$$

and combines the effects of electronic- and thermal-transport properties in one quantity.

Both, κ_e and κ_L enter the figure of merit in Eq. (17). Therefore, ZT does not directly reveal the properties related only to the electronic structure. Seemingly, the Seebeck coefficient might be a better indicator of changes in the electronic structure. In particular, the transport integral ν/τ [Eq. (10)] entering S is very sensitive on changes in the electronic structure close to the Fermi energy. This is, however, not the complete truth. Another, well-known effect based on the lattice vibrations influences S, namely, the so-called *phonon drag*. It is related to C_L and a rough estimation results in a maximum value of about $-86\ \mu\text{V K}^{-1}$.[20] Although this value may be much too large, the effect itself cannot be neglected and is most pronounced at temperatures around $T/\Theta_D \approx 0.2$.

III. EXPERIMENTAL DETAILS

The $\text{Co}_2\text{Ti}Z$ (Z=Si, Ge, Sn) samples have been prepared by arc melting of stoichiometric amounts of the elements. To remove oxygen contaminations the sample chamber was flushed with Ar and afterward evacuated. This process was repeated three times before each melting. To remove final trays of oxygen, Ti was heated close to evaporation inside the vacuum chamber before melting the compounds. To ensure the homogeneity, the samples were flipped before each new melting step. The resulting polycrystalline ingots were afterward annealed in evacuated quartz tubes for 21 days. This procedure resulted in samples exhibiting the $L2_1$ structure. Bars of about $(2\times2\times8)\ \text{mm}^3$ were cut from the pellets and polished before measuring. For powder investigations, the remainder was crushed by hand using a mortar.

The crystalline structure of the compounds was investigated by x-ray powder diffraction (XRD) using Mo $K\alpha$ radiation (Bruker D8 Advance). Complementary, temperature-dependent XRD experiments were performed at the XRD beamline at the bending magnet D10 of the Brazilian Synchrotron Light Laboratory (LNLS). For details about the characteristics of the beamline see Ref. 25.

For the inspection of the surface a scanning electron microscope (SEM) (Jeol JSM-6400) equipped with an EDX-detection system (Surface Concept GmbH) was used. The samples were measured in a vacuum of 3×10^{-6} mbar. An acceleration voltage of 20 kV was applied and an inspection angle of 35° was set up. For the correction the ZAF method was applied. For the image acquisition the digital image processing system and for the quantitative chemical analysis the program WINEDS 4.0 were used.

The measurements of the Seebeck coefficient, thermal conductivity, and resistivity were carried out with a physical property measurement system (model 6000 Quantum Design, with the options P400, P600, and P640) from 2 to 400 K. The bars have been contacted by copper stripes, that were wrapped around the sample to homogenize the current passing through. Additionally, the stripes were glued to the sample with a silver epoxy paste to improve the contact. The samples were polished before contacting to remove oxide layers which may have formed between the synthesis and the measurement. The sample chamber was flooded with He and afterward evacuated. The thermoelectric properties were measured at a pressure of about 1.2×10^{-4} mbar by a standard four-point ac method. An additional correction term for the heat loss at the heating shoes was introduced and applied to the thermal-conductivity data as it was suggested by Müller *et al.*[26] and Quantum Design.[27] The electrical conductivity and the Seebeck coefficient were determined in the temperature range of $340 < T < 900$ K using the RZ2001i unit of Ozawa Science, Japan. Both parameters were recorded simultaneously as a function of temperature in an Ar atmosphere. The Seebeck coefficient was measured by a steady-state method and the electrical conductivity by the dc four-point method. The magnetic properties were investigated by a superconducting quantum interference device (SQUID, Quantum Design MPMS-XL-5) using nearly spherical pieces with a weight of about 8 mg.

For the HAXPES investigations, the sample bars were

TABLE I. Band-structure parameters for Co_2TiZ (Z=Si, Ge, Sn) compounds. Given are the relaxed lattice parameter a, the bulk modulus B, the size of the hybridization gap ΔE_{hyb}, the valence-band maximum of the minority states with respect to the Fermi energy E_{VBM}, and the size of the band gap ΔE_{HMF} of the minority states.

Z	a (Å)	B (GPa)	ΔE_{hyb} (eV)	E_{VBM} (eV)	ΔE_{HMF} (eV)
Si	5.758	207	2.01	−0.61	0.785
Ge	5.850	190	2.81	−0.40	0.569
Sn	6.093	169	2.16	−0.22	0.504

fractured *in situ*. This assures that the samples are free of oxygen contaminations. The HAXPES experiments were performed at the beamline BL15XU of SPring-8 (Japan). The photon energy was fixed at 5.947 keV using a double-crystal monochromator and a Si(333) postmonochromator. The emitted photoelectrons were analyzed for their kinetic energy and detected by means of a hemispherical analyzer (VG Scienta, R4000). The overall energy resolution (monochromator plus analyzer) was set to 250 meV, as verified by spectra of the Au valence band (VB) at the Fermi energy. The angle between the electron trajectory to the spectrometer and photon propagation is fixed at 90°. The photons are p polarized, that is, the electric field vector is in the plane of incidence and always pointing in the direction of the electron detector. A near normal-emission (θ=8°) detection angle was used. This corresponds to an angle of incidence of $\alpha=90° -\theta=82°$. One should notice, however, that these angles might not be that sharply defined for the fractured samples but rather vary across the area of the light spot due to surface roughness.

IV. RESULTS AND DISCUSSION

A. Results of the first-principles calculations

The basis for the calculation of the thermoelectric properties is the calculated electronic structure. From that basis the transport properties are calculated. As starting point, the electronic structure of the Co_2TiZ compounds with Z=Si, Ge, or Sn was calculated using the FLAPW method as described above. The lattice parameter a of the compounds was optimized before calculating the electronic-structure and transport properties. The resulting lattice parameters are summarized in Table I together with the accompanied bulk moduli B. Both quantities were found from an equation of state fit of the total energy as function of the volume of the primitive cell. The lattice parameter increases with increasing ordinal number of the main group element. At the same time, the bulk modulus decreases. The decrease in B with increasing a is caused by the weakened interaction between the Co atoms. At larger Co-Co distances the Co d electrons have less overlap.

In spin-polarized calculations, these compounds turn out to be half-metallic ferromagnets as was previously shown by various authors.[4,5,28–30] The band structure of Co_2TiGe is shown in Fig. 1 as the representative for all three compounds. A band gap in the minority states occurs at the Fermi energy ϵ_F. This minority gap is characteristic for half-metallic materials. The size of the gap amounts to ΔE_{HMF} =569 meV and the top of the minority valence band is located 400 meV below ϵ_F. The majority-band structure is metallic with a single band crossing ϵ_F in the Δ direction. Due to the band gap in the minority states, the magnetic moment is integer and has a value of exactly $2\mu_B$ for the primitive cell. A closer analysis shows that the magnetic moment is mainly located at the Co atoms. That means, each of the two Co atoms in the primitive cell carries a magnetic moment of about $1\mu_B$. Details of the calculated band structure and the local magnetic moments were just confirmed by the experimental investigation of the spin-resolved unoccupied density of states.[31]

Besides the minority gap, a pronounced hybridization gap is observed above the low-lying s bands at approximately −10 eV. This indicates a strong bond between the Ge atoms and the surrounding Co atoms. The latter themselves form a very stable simple cubic sublattice. Consequently, the Ge atoms are well fixed in the CsCl-like positions of the Co sublattice and Ge and Ti atoms cannot easily be exchanged. Hence, a $B2$-type disorder as often observed in Al-containing Heusler compounds becomes improbable.

The Co_2TiZ compounds with Z=Si or Sn have very similar electronic structures. In particular, they are also half-metallic ferromagnets with a magnetic moment of exactly $2\mu_B$ for the primitive cell. The main differences appear due to the change in the lattice parameter. This change causes a slight variation in the slope of the dispersion curves $E(k)$. As a consequence, the size of both the minority gap as well as the hybridization gap are slightly different. These parameters are compared in Table I. The hybridization gap ΔE_{hyb} is slightly smaller in the Si- or Sn-based compounds compared

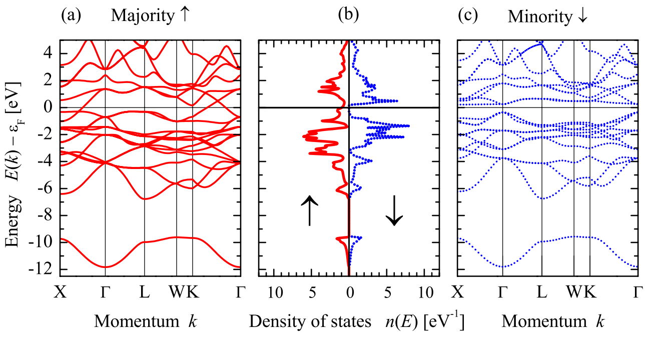

FIG. 1. (Color online) Spin-resolved electronic structure of Co_2TiGe. Shown are the band structures for the (a) majority and (c) minority electrons together with the (b) density of states.

to the case of Ge. The size of the minority gap ΔE_{HMF} decreases with increasing ordinal number of the main group element. It is smallest in the Sn-based compound that has the largest lattice parameter. In Co_2TiSn, the Fermi energy is located close to the middle of the minority-band gap whereas ϵ_F is shifted toward the conduction-band minimum of the minority states in Co_2TiSi and Co_2TiGe.

So far the electronic structure of the ferromagnetic (FM) state was calculated. The question arises how it is influenced and changed when approaching and crossing the magnetic phase transition. In a simple model of localized moments one may assume that the minority and majority states become mixed. In the investigated compounds, neither the moment at the Ti atoms nor that at the Co atoms are completely localized. Therefore, localized models may fail.

The *disordered local-moment* (DLM) technique[32] is a powerful approach to derive at solutions without a net magnetic moment—but with nonvanishing individual moments—in the primitive cell. In the DLM case, two identical atoms with opposite spin polarization are set at each site of the cell and the charge distribution is found from the coherent-potential approximation.

DLM calculations were performed for the Co_2TiZ compounds but it was not possible to stabilize individual magnetic moments in the investigated systems. That is, the moment at the Co sites vanished in the self-consistent DLM approach. This demonstrates that the compounds behave completely itinerant and underlines another time that localized magnetic moments are not a necessary condition for the appearance of half-metallic ferromagnetism. Further it should be noted that the density of the minority states vanishes identically in the investigated compounds due to their half-metallic character. A simple mixing of densities would therefore not at all change the averaged transport properties from the purely electronic point of view. An alternative approach is the use of nonpolarized (spin-polarized) calculations. In the following, the results from such non-spin-polarized calculations—often attributed paramagnetic—are compared to the results from the spin-polarized calculations.

Figure 2 compares the total density of states of all three investigated compounds for energies close to ϵ_F. The energy range is reduced to display the states in the vicinity of the Fermi energy because the states at these energies are most interesting for the transport properties. The electronic structure was calculated for the non-spin-polarized (PM) and the spin-polarized (FM) cases. The total density of states is the sum of the majority and minority states for the spin-polarized calculation (see Fig. 1 for the spin-resolved densities of Co_2TiGe).

The changes in the density of states are obvious if comparing the spin-polarized and nonpolarized cases. The density at ϵ_F is considerably larger in the PM case for all three compounds. The main difference appears from the unoccupied density of states in the FM calculation. In Co_2TiGe, the states at about 0.5 eV above ϵ_F are unoccupied minority states (compare Fig. 1). In the PM state one has no exchange splitting and those states are found below ϵ_F. For Co_2TiSi and Co_2TiSn, the high density of states close to ϵ_F in the PM states is derived in the same way. From the differences of the electronic structure of the FM and PM states one expects also differences in the calculated transport properties.

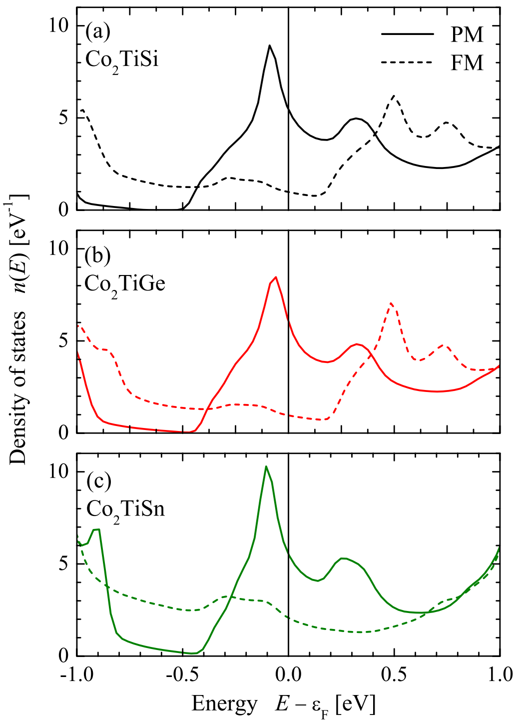

FIG. 2. (Color online) Total density of states of Co_2TiZ (Z = Si, Ge, Sn). Displayed are the results of non-spin-polarized (PM) and spin-polarized (FM) calculations.

Figure 3 compares the ferromagnetic and non-spin-polarized band structure of Co_2TiGe in the vicinity of the Fermi energy. Obviously, one band is crossing in the spin-polarized case in the Fermi energy and contributes to the transport properties. This band has t_{2g} character at Γ and along the fourfold Δ direction. In the Σ direction with lower, twofold rotational symmetry it has an admixture of e_g character that connects to the K point. Both, majority and minority bands exhibit a Van Hove singularity (saddle point) in the

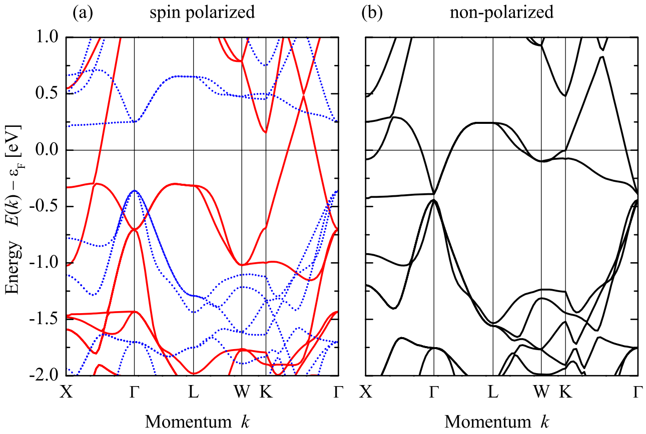

FIG. 3. (Color online) Comparison of the band structure of Co_2TiGe close to ϵ_F. Shown are the band structures from (a) spin-polarized and (b) nonpolarized calculations. Note that majority (full lines) and minority states (dotted lines) are shown in (a) in one plot for better comparison with the nonpolarized case.

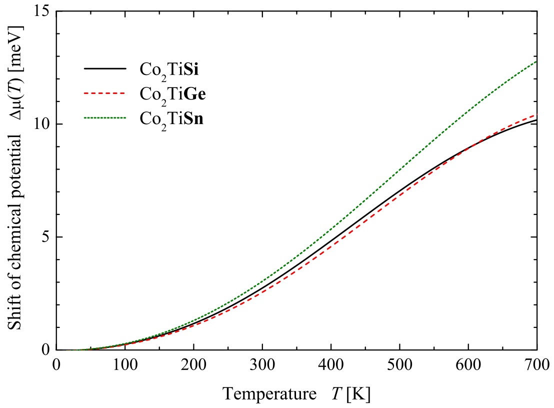

FIG. 4. (Color online) Temperature dependence of the chemical potential. The shift $\Delta\mu(T)$ of the chemical potential with temperature T was calculated for the spin-polarized electronic structure of Co_2TiZ with Z=Si, Ge, or Sn.

Λ direction at about 0.3 eV below and 0.66 eV above ϵ_F, respectively. In the nonpolarized case, where the exchange splitting is removed, only one Van Hove singularity remains at 0.24 eV above ϵ_F. Further it is seen that much more bands are crossing the Fermi energy and contribute to the transport. Thus it is expected that the electric resistivity in the non-spin-polarized state is lower compared to the ferromagnetic state.

As mentioned in Sec. II A, the chemical potential μ changes with temperature. Figure 4 illustrates the effect of the temperature on the chemical potential as calculated for the three compounds under investigation. The shift $\Delta\mu(T)$ is calculated for the spin-polarized electronic structure. At low temperatures the shift of μ follows a parabolic shape expected from Eq. (12). Clear deviations are obvious for temperatures of above 400 K. The shift is nearly the same for the compounds with Z=Si or Ge whereas it is considerably stronger in the Sn-containing compound. This effect is clear from the differences in the density of states as explained above.

In the next step, the conductivity was calculated. Figure 5 compares the conductivity integrals σ/τ calculated for the spin-polarized and nonpolarized electronic structure. Obviously, the conductivity integral is larger and exhibits a slightly stronger temperature dependence in the nonpolarized case. This is expected from the higher density of states at the Fermi energy (see Fig. 2). The weak dependence of the calculated conductivity integrals σ/τ on temperature is typical for metals. Overall the changes are not very large because all influences of the relaxation time τ are omitted.

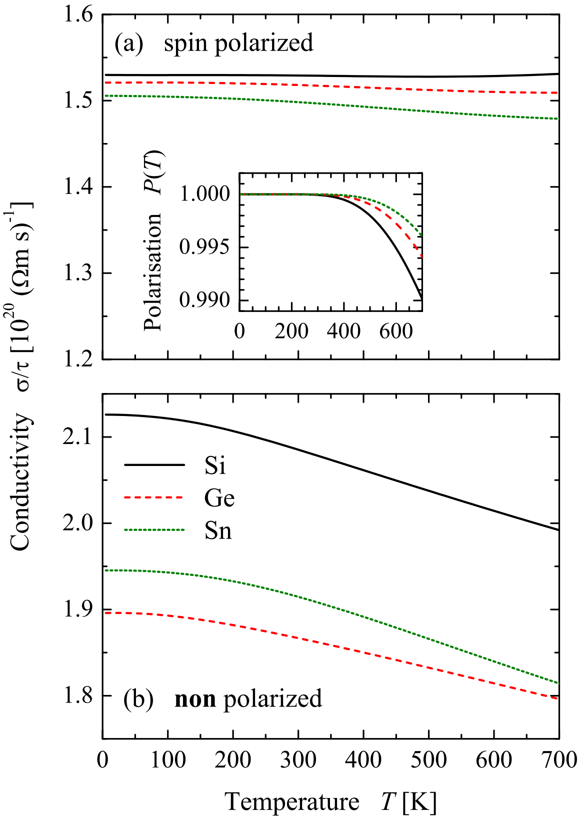

FIG. 5. (Color online) Temperature dependence of the conductivity integral σ/τ. The temperature dependence of was calculated for the (a) spin-polarized and (b) nonpolarized electronic structure of Co_2TiZ with Z=Si, Ge, and Sn. The inset in (a) shows the expected spin polarization of the electric current if neglecting the magnetic phase transition.

The inset of Fig. 5(a) shows the expected temperature dependence of a spin-polarized current for the case that no depolarization effects due to the temperature dependence of the magnetization occurs. That is, it is assumed that the materials stay completely in the half-metallic ferromagnetic state and no mixing of minority and majority states occurs over the entire temperature range. For low temperatures the current is completely carried by majority electrons and 100% spin polarized. A discernible reduction in the polarization of the current is only observed at temperatures above 300 K. It is interesting to note that the Sn-based compound exhibits at high temperatures the highest polarization $P(T)$ even it has the smallest minority gap. This demonstrates that the temperature dependence of the spin polarization of the current is not simply determined by the size of the minority gap but depends more critically on details of the electronic structure close to the Fermi energy. For Co_2TiSn, the Fermi energy is found in the middle of the minority-band gap and, indeed, farther away from the minority-band edges.

Figure 6 displays the calculated Seebeck coefficient S and figure of merit ZT_e. The calculations were performed for the spin-polarized (FM) as well as the nonpolarized (PM) electronic structure. Here, ZT_e contains only the electronic thermal conductivity κ_e. The overall value of ZT, however, will also depend on the lattice contribution κ_L to the thermal conductivity that may even exceed the electronic part in magnitude. According to Eq. (17) it is expected that ZT_e overestimates the overall value. The calculation of the overall ZT may become very complicated due to the influences of the different relaxation times entering the equations for κ_e and κ_L. For the present purpose it is sufficient to compare the values of ZT_e. It is clear from Fig. 6 that ZT_e and thus ZT is different for the non-spin-polarized and spin-polarized calculations. This observation will hold even if accounting for a reduction in ZT by the influence of κ_L.

In the spin-polarized calculations the Seebeck coefficient is positive and increasing at low temperatures for all three

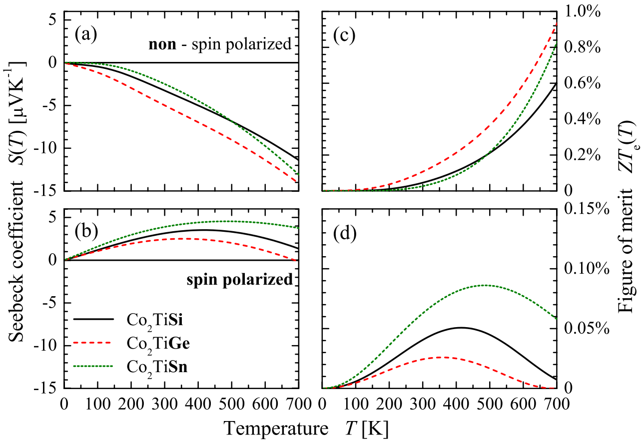

FIG. 6. (Color online) Calculated temperature dependence of the Seebeck coefficient and figure of merit. The dependence of S [(a) and (b)] and ZT_e [(c) and (d)] on temperature T was calculated for the spin-polarized (FM) and nonpolarized (PM) electronic structure of Co$_2$TiZ with Z=Si, Ge, and Sn. Note the different scale of ZT_e in the FM [(c)] or PM [(d)] case.

compounds. This is expected from simple models that estimate the Seebeck effect from the change in the density of states close to the Fermi energy. The behavior at low temperatures is clear, as only one band with a free-electronlike shape is crossing ϵ_F. At higher temperatures, however, S decreases with T. This is due to the increasing influence from lower-lying bands. These flat bands are clearly seen at about −100 meV in Fig. 1 for Co$_2$TiGe and appear as maxima in the density of states in Fig. 2. This demonstrates that simple free-electron-based calculations are not sufficient to explain the Seebeck coefficient. The calculated Seebeck coefficient of all three compounds is negative with increasing absolute value in the nonpolarized case. Here, several different bands that are crossing the Fermi energy contribute to the transport properties. This underlines another time that the Seebeck coefficient as calculated from Eq. (9) is a measure for the band dispersion rather than the density of states. Indeed, it averages over all contributing bands close to the Fermi energy.

The calculation of $S(T)$ in Fig. 6 already includes the temperature shift of the chemical potential $\mu(T)$. The chemical potential may be changed also by other effects. Small deviations from the nominal composition will change the electron concentration resulting in a shift of the Fermi energy and accordingly of $\mu(T)$. The same is true for small amounts of impurities or disorder in the samples. To estimate the effect of such changes in μ, the Seebeck coefficient was calculated as a function of the chemical potential for a fixed temperature of 300 K. The results for the spin-polarized and nonpolarized electronic structure of Co$_2$TiGe are compared in Fig. 7.

From Fig. 7 it is obvious that a shift of μ by about −100 or +150 meV is already enough to change the sign of the Seebeck coefficient in the ferromagnetic state. Large changes are also observed if the chemical potential in the non-spin-polarized state is shifted to lower values. At −100 meV the Seebeck coefficient is one order of magnitude larger than at the nominal zero position of μ. These findings demonstrate that already small changes in the electronic structure will change the Seebeck coefficient considerably.

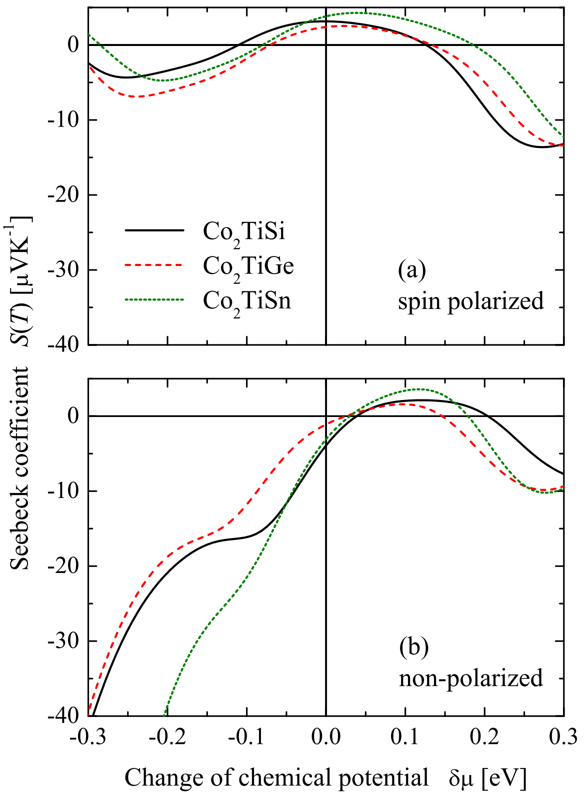

FIG. 7. (Color online) Dependence of the Seebeck coefficient of Co$_2$TiZ compounds on the chemical potential. The dependence of $S(\mu)$ was calculated for T=300 K for the spin-polarized and the nonpolarized cases.

In the next step the vibrational properties of the investigated compounds were studied. The results of the phonon calculations are based on the spin-polarized electronic-structure calculations. Figure 8 compares the calculated phonon dispersion $h\nu(q)$ and the accompanied density of states $g(\omega)$ of the Co$_2$TiZ compounds with Z=Si, Ge, and Sn. The largest bandwidth is obtained for the Si-based compound. In that compound, the upper energies are determined by the optical modes arising from the vibrations of the Si atoms. The bandwidth decreases with increasing mass of the main group elements and is lowest in the compound based on Sn. The topmost separate bands in Co$_2$TiGe arises from the optical modes related to the vibrations of the Ti atoms. The separation of those bands is less pronounced in Co$_2$TiSn.

Figure 9 displays the temperature dependence of the phonon part $C_L(T)$ of the specific heat calculated from the phonon densities shown in Fig. 8. The temperature dependence of the heat capacity was used to determine the Debye temperatures Θ_D of the compounds. The results for Θ_D are compared to the average phonon energies $\hbar\bar{\omega}$ in Table II. The average phonon frequency is calculated from the density of states by $\bar{\omega}=\int \omega g(\omega) d\omega$. Both quantities show the same behavior and decrease with increasing mass of the Z element. This is, indeed, expected from the behavior of the phonon density of states of the different compounds.

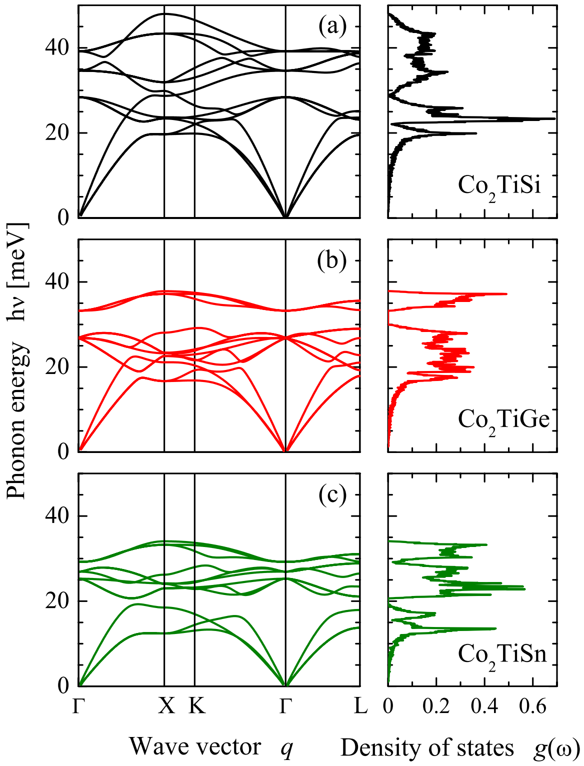

FIG. 8. (Color online) Phonon properties of Co_2TiZ compounds. Shown is the phonon dispersion $h\nu(q)$ and the accompanied density of states $g(\omega)$ for Z=Si, Ge, and Sn.

B. Structure and composition

The crystal structure of the samples was investigated by powder XRD using Mo $K\alpha$ as well as synchrotron radiation. The obtained diffraction patterns are shown in Fig. 10. All compounds exhibit a cubic structure and no impurity phases were detected within the limits of the method. The fcc typical (111) and (200) reflexions are clearly detected for the Si- and Sn-based compounds. This gives advice on the cubic $L2_1$ structure (space group: $Fm\bar{3}m$) as main phase of those compounds. The (200) reflexion is absent, however, in Co_2TiGe when Mo $K\alpha$ radiation is used. The absence of this reflexion might point on a $B32$-type disorder (NaTl-like structure with $Fd\bar{3}m$ symmetry).[33] On the other hand, it has to be noted that the contributing elements are all from the same row of the periodic table and therefore have similar scattering factors. To prove the influence of the scattering factors a XRD experiment[34] was performed with the pattern taken at $h\nu$ $=7111.96$ eV.

TABLE II. Phonon properties of Co_2TiZ (Z=Si, Ge, Sn) compounds. Given are the Debye temperature Θ_D and the temperature equivalent of the average phonon frequency $\bar{\omega}$.

Compound	Θ_D (K)	$\hbar\bar{\omega}/k_B$ (K)
Co_2TiSi	469	349
Co_2TiGe	395	295
Co_2TiSn	370	275

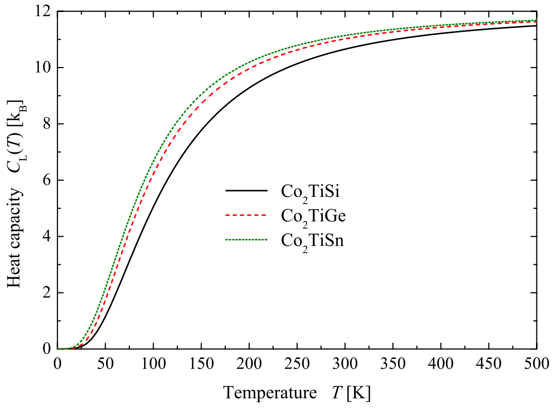

FIG. 9. (Color online) Calculated lattice specific heat of the Co_2TiZ compounds.

A Rietveld refinement of the experimental data was performed assuming an ordered $L2_1$ structure as well as different disordered structures. The obtained cubic lattice parameter a does, indeed, not depend on the assumption of disorder in the cubic structures. The resulting values measured at room temperature using Mo $K\alpha$ as well as synchrotron radiation are summarized in Table III and compared to calculated values as well as values previously published by other authors. The lattice parameters are in good agreement with previously reported ones.

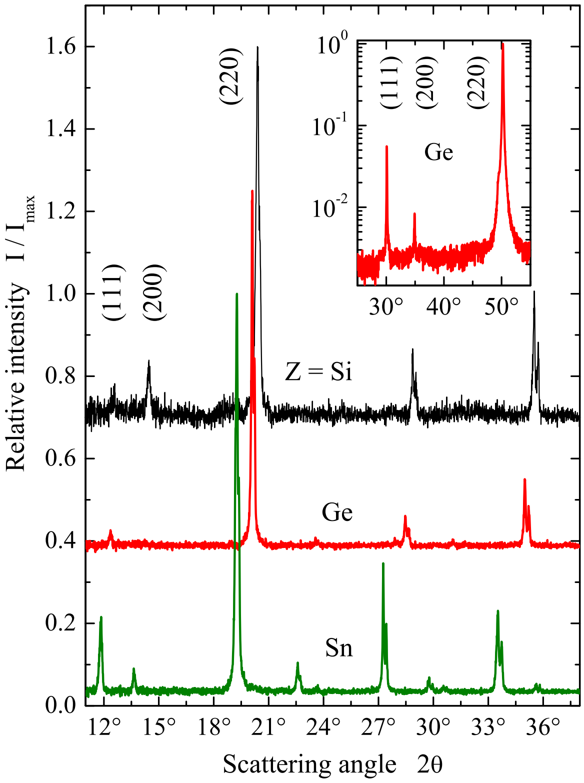

FIG. 10. (Color online) Powder XRD of the Co_2YZ compounds with Z=Si, Ge, Sn. The diffraction pattern are measured at room temperature with Mo $K\alpha$ radiation. The inset displays a diffraction pattern of Co_2TiGe measured with a photon energy of $h\nu$ ≈ 7.1 keV. Note the logarithmic intensity scale of the inset.

TABLE III. Lattice parameters of Co_2TiZ compounds with Z = Si, Ge, Sn. The 0 K values are extrapolated from a fit of the temperature-dependent data.

Compound	T (K)	a_{exp} (Å)	a_{calc} (Å)	a_{lit} (Å)
Co_2TiSi	300	5.849	5.758	5.743[a]
Co_2TiGe	300	5.82		5.831[b]
	20	5.808		
	0	5.8069	5.850	
Co_2TiSn	300	6.066		6.076[c]
	20	6.053		
	0	6.0527	6.093	

[a] Reference 35.

[b] Reference 36.

[c] Reference 37.

Furthermore, the temperature dependence of the lattice parameter of the Ge- and Sn-containing compounds was studied using synchrotron radiation. The results are displayed in Fig. 11. In both compounds the lattice parameter exhibits a nonlinear dependence and decreases by about 0.25% when reducing the temperature from 300 to 20 K. The data were fitted to a $a(T)=a_0(1+\alpha T+\beta T^2)$ model for the thermal expansion. For both compounds, the linear-expansion coefficients are $\alpha \approx 5\times 10^{-6}$ K^{-1} and the quadratic terms are in the order of $\beta \approx 10^{-8}$ K^{-2}. The order of magnitude of both coefficients is typical for most metals. The calculated values a_{calc} are slightly larger compared to the extrapolated values at 0 K. This is typical for volume optimizations using GGA as exchange-correlation functionals. The small deviation of about 0.5%, however, does not change the results of the calculations of the electronic structure.

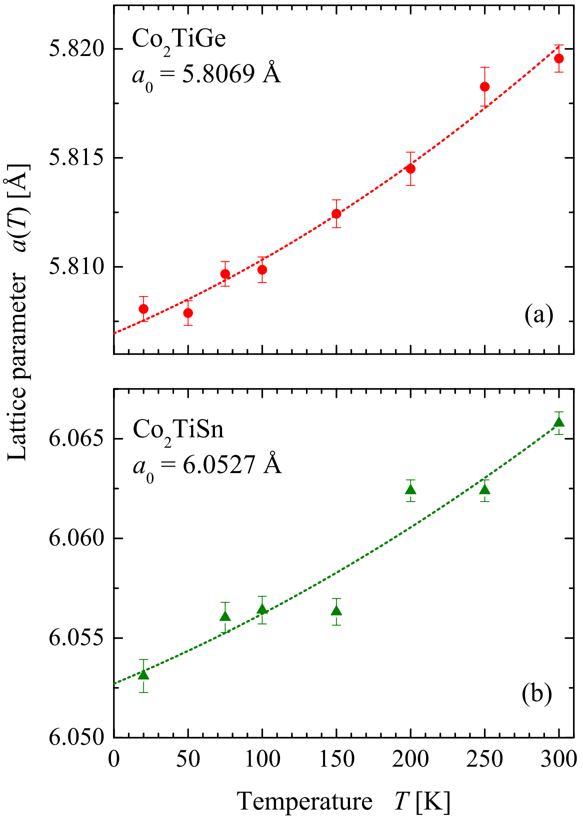

FIG. 11. (Color online) Temperature dependence of the lattice parameter of Co_2TiGe and Co_2TiSn. The photon energy was set to about 7.1 keV. Lines are the results of a nonlinear curve fitting (see text).

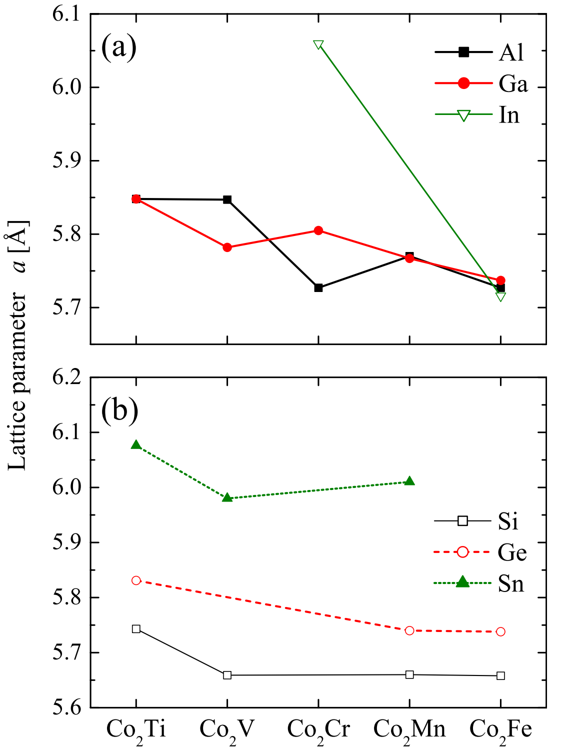

FIG. 12. (Color online) Shown are the lattice parameters of the Co_2YZ compounds and their change with a fixed Y and a varying Z position. (a) The Y position is occupied by a $3d$ transition metal and Z with an element of the IV main group of the periodic table. Data were taken from Refs. 5 and 38–57. (b) The Y position is occupied by a $3d$ transition metal and Z with an element from the III main group of the periodic table. Data were taken from Refs. 35, 39–44, 46, and 58–67.

In Fig. 12 the lattice parameters for Co_2YZ compounds are shown. On the x axis the transition metals at the Y position are displayed with increasing atomic numbers from to Ti to Fe. In part (a) of Fig. 12 the Z position is fixed with Z = Al, Ga, and In and in part (b) the Z position is fixed with Z = Si, Ge, Sn.

For the compounds Co_2YZ (Z = Al, Ga, In) displayed in Fig. 12(a) no trend concerning the exchange at the Y position can be given. The difficulties arise due to the lack of lattice parameters for Co_2YIn compounds and the sublattice intermixing in Co_2TiZ, Co_2MnZ, and Co_2FeZ with (Z = Al, Ga, In). Although it is observable that the lattice parameter are declining with an increasing atomic number at the Y position. An increase in the lattice parameter with the increase in the atomic number from Al to In is not observed. Although this is expected due to the increase in the atomic radius of the elements in the group.

A trend in part (b) of Fig. 12 is observed even though the data for Co_2VGe, Co_2CrZ, and Co_2FeSn compounds is not available. For all Co_2YZ (Z = Si, Ge, Sn) systems the in-

TABLE IV. Chemical composition of the Co_2TiZ compounds. Values are given in at. %. R gives the ratio $Co_2:Ti:Z$.

Element	Co_2TiSi	Co_2TiGe	Co_2TiSn
Co	49	50	53
Ti	23	23	25
Z	28	27	22
R	2:0.94:1.14	2:0.92:1.08	2:0.94:0.83

crease in the lattice parameter is about 0.1 Å when Si is exchanged with Ge and 0.25 Å for the exchange of Ge with Sn for a given element at the Y position. The cell parameter is decreasing from Co_2TiZ (Z=Si, Ge, Sn) to Co_2VZ (Z=Si, Ge, Sn). The influence of atoms with higher atomic numbers at the Y position is small compared to the change from Ti to V. The experimentally determined lattice parameters for Co_2TiSn and Co_2TiSi follow the observed trends very well. The cell parameter values for Co_2TiGe are smaller than expected.

EDX spectroscopy was performed on the compounds. The results of the quantitative chemical analysis are presented in Table IV. All the 2:1:1 compositions are within the experimental[68] error of 5%. On the edges of the samples small Al impurities were found. The Al is introduced by the glue, that was used for the mounting of the sample. In Fig. 13 the SEM micrograph of the Co_2TiSi surface is displayed. Two segregations are identified at the surface. The first one denoted with A at the cutting edges is the before mentioned Al. It is found for all three compounds. The second segregation denoted with B is an accumulation of elementary Si. The Si impurity covers an area of about 4000 μm^2. The Ge- or Sn-containing compounds exhibit a uniform composition.

C. Hard x-ray photoelectron spectroscopy

High-energy photoelectron spectroscopy was carried out to prove the calculated electronic structure. Figure 14 shows a wide energy scan of Co_2TiSi. No foreign contents or impurities are detected. Only a very small contribution of CO at the surface (O 1s at −530 eV and C 1s at −286 eV) of the sample is visible.

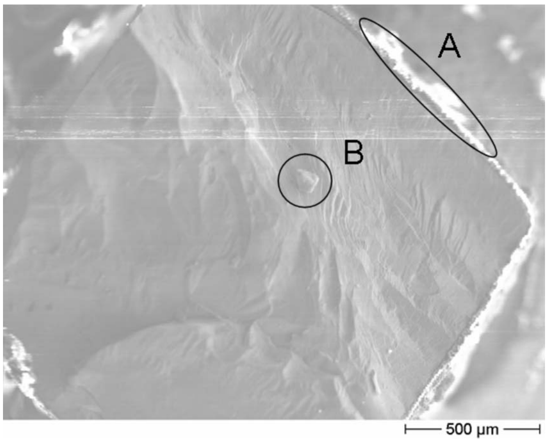

FIG. 13. SEM micrograph of Co_2TiSi. A and B mark Al and the Si impurities, respectively.

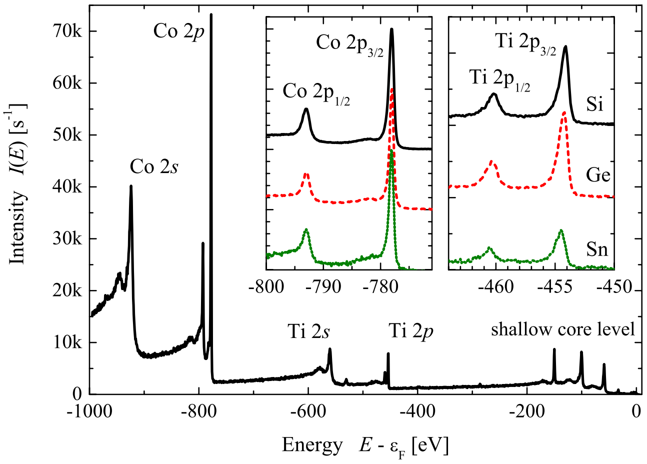

FIG. 14. (Color online) Hard x-ray core-level spectra of Co_2TiZ (Z=Si, Ge, Sn). Shown is a wide energy scan spectrum of Co_2TiSi. The inset displays the 2p core level of Co and Ti of the compounds with Z=Si, Ge, Sn in more detail. The measurements were performed at T=300 K using an excitation energy of 5.947 keV.

A more detailed analysis was performed on the 2p core level of Co and Ti that are shown in the inset of Fig. 14. Both states exhibit a clear spin-orbit splitting $\Delta_{SO}=E(p_{3/2})-E(p_{1/2})$ that is summarized in Table V. The splitting does not change with composition within the resolution of the experiment and agrees well with the calculated values of 14.8 and 5.8 eV for Co and Ti, respectively. It is worth noting that neither calculated nor measured binding energies exhibit pronounced chemical shifts between the compounds, as expected. The overlap of several peaks with peaks of other elements, for example, Co 2p and Sn 3p does not allow a quantitative analysis of the compounds.

The spin-orbit splitting of the Co 2p states as determined by x-ray absorption spectroscopy[31] (5.7 eV for Ti and 15.1 eV for Co) is close to the values determined by x-ray photoemission spectroscopy (XPS). The difference results from the fact that the final state involves the band broadening of the 3d states just above the Fermi edge. This peak broadening also does not allow to determine a Co:Ti intensity ratio that can be compared with XPS. However, all three compounds showed similar intensity ratios for Co and Ti spectra.

Figure 15 compares the spectra of the shallow core level of the compounds in the energy range from −180 eV up to

TABLE V. Intensity ratios and spin-orbit splitting of the Co and Ti 2p core states in Co_2TiZ compounds. The intensity ratios $R=I(\mathrm{Co})/I(\mathrm{Ti})$ are taken from the 2s and 2$p_{3/2}$ states and have an uncertainty of 5%, mainly due to nearby other transitions and satellites. The spin-orbit splitting Δ_{SO} is given in eV.

Compound	Δ_{SO} Co 2p	Δ_{SO} Ti 2p
Co_2TiSi	14.94	6
Co_2TiGe	14.91	6.1
Co_2TiSn	14.95	6

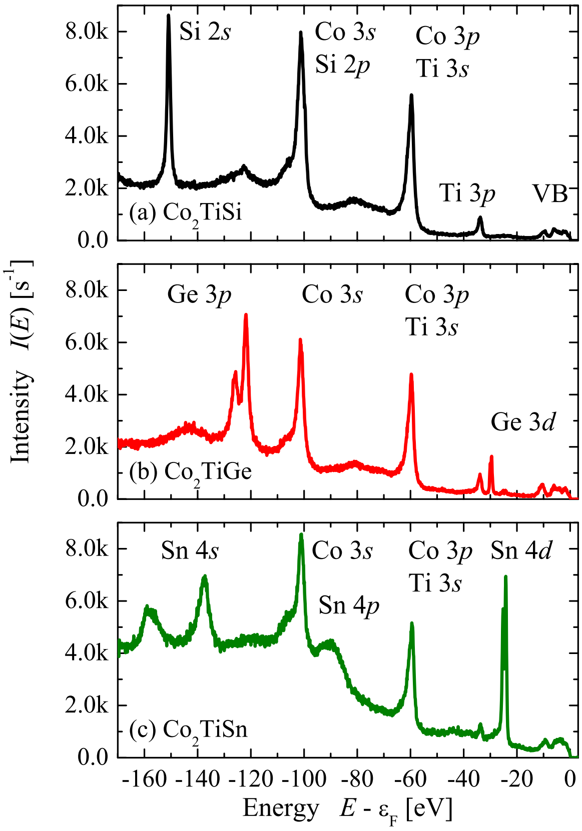

FIG. 15. (Color online) Hard x-ray semicore-level spectra of Co_2TiZ (Z=Si, Ge, Sn). The Ti $3p$ states and the valence band (VB) are only marked in (a), other unassigned features in the spectra are metallic satellites of the nearby direct transitions. The measurements were performed at $T=300$ K using an excitation energy of 5.947 keV.

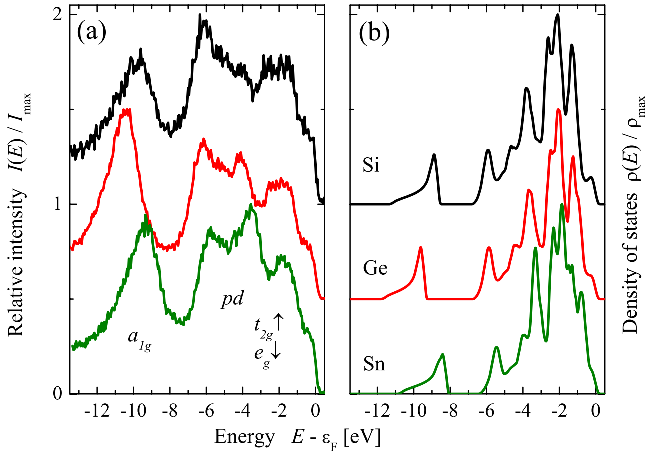

FIG. 16. (Color online) Hard x-ray valence-band spectra and density of states of Co_2TiZ (Z=Si, Ge, Sn). (a) shows the valence-band spectra and (b) the calculated density of states. The measurements were performed at $T=300$ K using an excitation energy of 5.947 keV. The density of states is convoluted by a Fermi-Dirac distribution and smoothed by Gaussians to reflect the finite temperature and resolution of the photoelectron emission experiment.

the Fermi energy in more detail. The very low intensity of the valence band compared to the shallow core level is obvious. Some states of the contributing elements exhibit nearly the same binding energies and cannot be resolved. These are Co $3s$ and Si $2p$ at about -101 eV as well as Co $3p$ and Ti $3s$ states at about -60 eV. In particular, the overlap of the latter two does not allow to use the shallow core level for determination of the stoichiometry of the investigated compounds. The increasing influence of the spin-orbit interaction becomes visible in the Ge-containing compound. The spin-orbit splitting of the Ge $3p$ and $3d$ states amounts to 3.98 and 0.55 eV, respectively, whereas the spin-orbit splitting of the Co or Ti $3p$ states is not resolved. The splitting of the Sn $4d$ states amounts to 1 eV. At the Co or Ti states noteworthily chemical shifts are not observed comparing the different compounds. The binding energies are the same within the experimental resolution.

Figure 16 displays the valence-band photoemission spectra and the calculated total density of states of the three compounds investigated here. For better comparison the density of states is convoluted by a Fermi-Dirac distribution ($T=300$ K) and smoothed by Gaussian with a width of 250 meV. The latter accounts for the experimental resolution but neglects, however, any broadening caused by lifetime effects. The photoemission spectra were taken at room temperature using an excitation energy of about 6 keV. It was previously demonstrated[69] that the cross section of the contributing states (s, p, and d) are nearly equal at this photon energy. This allows easily a direct comparison of the photoemission spectra and the calculated density of states.

The main features of the valence-band spectra of the Co_2TiZ compounds agree well with the calculated density of states. The characteristic Heusler *sp* hybridization gap (around -7 eV) and the contributions of the a_{1g} states arising from the s electrons of the main group element are clearly resolved. The largest gap is obtained for Z=Ge. Both, the size of the gap and the position of the a_{1g} band maximum follow the same trend in the spectra and the density of states. The absolute positions are shifted due to the hole effect. The shorter lifetimes of holes several electron volt below the Fermi energy result in an energy shift in the spectra compared to the ground-state density of states. The maximum at about -4 eV arises from a *pd* hybridization of Co d states with p states of the main group element. With increasing Z of the main group element, its intensity increases strongly and it shifts toward the Fermi energy. The increase in the intensity when changing the main group element is a typical cross-section effect. The group of bands at -2 eV consist of majority t_{2g} and minority e_g states. The width of these bands is considerably largest in the Si-containing compound and decreases for the Ge- and Sn-containing compounds. The electronic-transport properties are mainly defined by the d states crossing the Fermi energy. In the present compounds these are steep e_g bands. The shift of the onset of the flat t_{2g} bands following these e_g bands from -0.95 to -0.7 eV if going from Si to Sn is clearly revealed in the spectra. Overall, the calculated electronic structure is confirmed by the photoelectron spectra.

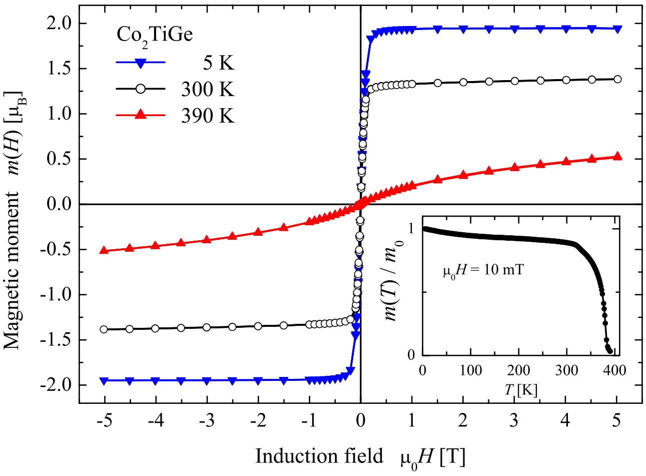

FIG. 17. (Color online) Magnetization of Co_2TiGe. Displayed are the hysteresis curves for $T=5$, 300, and 390 K. The inset shows the temperature dependence measured in an induction field of $\mu_0H=10$ mT.

D. Magnetic properties

In a first step toward the magnetic and thermoelectric properties, the magnetic behavior of the compounds was examined. This is important in the case of Co_2TiZ, because the band structure is influenced strongly by the type of magnetic order. Therefore, the Curie temperature T_C and the magnetic moment were determined. The Co_2-based Heusler alloys that are half-metallic ferromagnets show a Slater-Pauling-type behavior for the magnetization what means that the saturation magnetization scales linearly with the number of valence electrons.[4,70] This results for all three compounds in a theoretical magnetic moment of $2\mu_B$ in the primitive cell.

Low-temperature magnetometry has been carried out by means of the SQUID to investigate the field dependence of the magnetization and to determine the Curie temperatures of the samples. Selected results are shown in Fig. 17. The total magnetic moments of the ferromagnetic samples, measured at 5 K and in saturation, are just below $2\mu_B$ for all three compounds (see Table VI).

The Curie temperatures T_C were determined by the temperature dependence of the magnetization measured in a small induction field of $\mu_0H=10$ mT. See the inset of Fig. 17 for Co_2TiSi as an example. The Curie temperatures are 380 K for both Co_2TiSi and Co_2TiGe, and 355 K for Co_2TiSn. These values fit the theoretical predictions for the Curie temperatures of Heusler compounds very well. An approximately linear dependence is obtained for Co_2-based Heusler compounds when plotting the Curie temperature of the known, $3d$-metal-based Heusler compounds as a function of their magnetic moment.[70] According to this plot a T_C between 300 and 400 K is expected. Kübler developed an *ab initio* method for calculating the Curie temperatures from the energies of spiral spin-density waves.[71] This method was applied to Co_2-based Heusler compounds.[72] The calculated results are in very good agreement with the values obtained here for the Co_2TiZ ($Z=$Si, Ge, Sn) compounds.

TABLE VI. Determinations of the Curie temperatures (T_C), the maxima of the resistivity (T_R), and the total magnetic moments m for the Co_2TiZ compounds.

Compound	T_C (K)	T_R (K)	m (μ_B)
Co_2TiSi	380 ± 5	370 ± 20	1.96
Co_2TiGe	380 ± 5	350 ± 30	1.94
Co_2TiSn	355 ± 5	360 ± 15	1.97

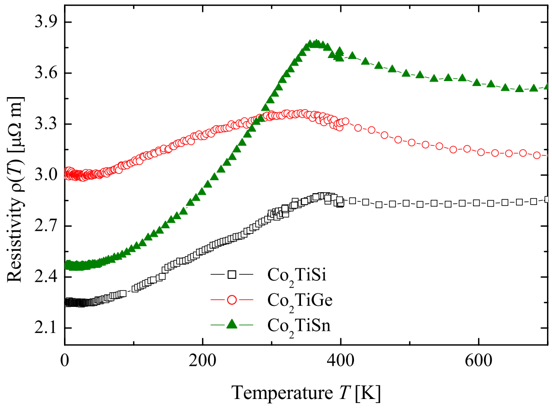

FIG. 18. (Color online) Measured temperature-dependent electrical resistivity of Co_2TiZ compounds with $Z=$Si, Ge, Sn.

In Table VI the measured Curie temperatures and the magnetic moments are summarized. The agreement between T_C from SQUID measurements and the temperature T_R of the resistivity maxima are obvious (see also Sec. IV E 1). The linear dependence reported in Ref. 70 yields values between 350 and 400 K. These agree with experimentally determined values and thus can be used as a rule of thumb to predict the Curie temperature. The values determined with the mean-field calculations[72] are a little higher than the values of the experiments. For the total spin magnetic moments the experimentally determined results by the SQUID agree very well with the data obtained from the calculations, they are at 5 K throughout about $2\mu_B$ as expected from the calculations with a half-metallic ferromagnetic ground state.

Further details of the magnetic structure, especially the site-resolved magnetic moments, are reported in Ref. 31. The Ti moment is small and shows antiparallel to the Co moment. Element-specific magnetic moments extrapolated to 0 K using SQUID data assume values of $-0.05\mu_B$ per Ti atom and $1.0\mu_B$ per Co atom. The ratio between orbital and spin moment is 0.06 for Co_2TiSi, 0.14 for Co_2TiGe, and 0.09 for Co_2TiGe.

E. Transport properties

1. Electrical resistivity

The resistivity data for temperatures from 2 to 400 K were obtained by a standard ac four-probe method and the data from 350 to 950 K were measured by a standard dc four-point method. Figure 18 shows the temperature dependence of the resistivity. A typical metallic behavior is observed for the low-temperature range from 2 K up to the Curie temperature. Above T_C, a decrease in the resistivity is observed. The

TABLE VII. Residual resistivity, relaxation time, and magnetic-scattering parameters of Co_2TiZ compounds with Z=Si, Ge, Sn. The residual resistivity ratios (R_{RR}) are determined from the resistivity at 2 and 300 K. The relaxation times τ are determined for temperatures far below (5 K) and far above (700 K) the Curie temperature. Physical units are given in the last column.

	Co_2TiSi	Co_2TiGe	Co_2TiSn	
R_{RR}	1.22	1.11	1.4	
τ (5 K)	2.9	2.2	2.7	fs
τ (700 K)	1.8	1.8	1.6	fs
ρ_0	2.23	3	2.45	$\mu\Omega$ m
c_R	119.1	29.9	12.5	pΩ m/K^n
n	1.47	1.7	1.96	
$\frac{d\rho}{dT}\|_{T\geq T_C}$	−0.5	−1.2	−1.1	nΩ m/K
ρ_m^*	0.9	0.8	1.7	$\mu\Omega$ m

decrease is very pronounced up to about 600 K and stays nearly constant at higher temperatures. This behavior leads to a pronounced anomaly of the resistivity at T_C. The resistivity measurements for Co_2TiSn agree well with previous findings of other authors.[73] Other than in many ferromagnetic materials, here the Curie temperature can be easily related to the maximum of the resistivity appearing at T_R. The determined values are 370, 350, and 360 K for Co_2TiSi, Co_2TiGe, and Co_2TiSn, respectively. These values agree well with the magnetic measurements.

In a first analysis, the residual resistivity ratios (R_{RR}) were determined from the resistivity measured at 2 and 300 K. The results are summarized in Table VII. Compared to paramagnetic metals, the resistivity at 300 K might be altered by the influence of the nearby phase transition at T_C. The mixture of spin polarized with nonpolarized states will reduce the resistivity already in that temperature range. This explains the rather small R_{RR} values. The Co_2TiGe sample exhibits the lowest ratio of the investigated compounds. This may be an indication for undetected antisite disorder in that sample. As mentioned above, the determination of the structure and possible disorder by XRD is complicated due to the similar scattering cross sections of the contributing atoms in that compound. Further, the relaxation time τ has been calculated for 5 K and for 700 K from the comparison of measured and calculated data. The temperatures were chosen to be well below and above the Curie temperature to exclude the influences of the magnetic phase transition. The values were calculated from the experimental resistivity ρ_{exp} and the calculated conductivity integral [see Eq. (7) and Figs. 5 and 19],

$$\bar{\tau} = \frac{1}{\rho_{exp}(\sigma/\tau)_{calc}} = \frac{(\rho\cdot\tau)_{calc}}{\rho_{exp}}. \qquad (18)$$

This yields an estimate for the mean relaxation time $\bar{\tau}$. The results are shown in Table VII. The obtained values are in agreement with the values reported for Bi_2Te_3 (Refs. 74 and 75) or Al (Ref. 76) regarding the large uncertainty of τ.

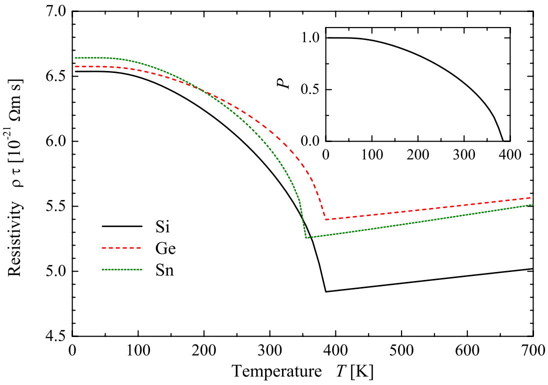

FIG. 19. (Color online) Calculated temperature dependent resistivity $\rho\tau$. The resistivity integral $\rho\cdot\tau$ of Co_2TiZ (Z=Si, Ge, Sn) is calculated from the conductivity integrals σ/τ in different magnetic states weighted by the magnetization in the molecular-field approximation. The inset shows the expected spin polarization of a current in Co_2TiSi that is proportional to the magnetization.

The maximum of resistivity at T_C is associated to the ferromagnetic to paramagnetic transition. Changes in the behavior of the resistivity at the Curie temperature are well known for the ferromagnetic metals Ni (Refs. 77 and 78) and Fe.[19] Most often they are best seen as singularity in the temperature derivative $\delta\rho/\delta T$ of the resistivity. A similar change was recently reported for Co_2TiAl,[79] a compound that is closely related to the Co_2TiZ compounds investigated here. Such changes are, however, very small compared to the changes observed for the investigated compounds. A real metal to insulator transition as explanation for the behavior of the resistivity at T_C is improbable. In that case one would expect a change in the resistivity by an order of magnitude. Maxima of the resistivity at T_C were reported for rare-earth metals where they occur in the resistivity along the c axis.[80,81] Much less pronounced deviations were reported for Gd compounds.[82]

Similar, cusp-type anomalies of the resistivity close to T_C were also reported for other Heusler compounds.[83,84] Other than in the present study, the investigated compounds Ni_2MnSn and Pd_2MnSn exhibit strong, localized magnetic moments at the Mn atoms whereas a similar localized moment is not possible at the Ti atoms of the Co_2TiZ compounds. According to Ref. 83 the maximum value of the magnetic-scattering resistivity ρ_m^* can be evaluated as the difference between $\rho_{pm}(0)$ and ρ_0, where $\rho_{pm}(0)$ is the estimated residual resistivity of the paramagnetic part and ρ_0 the residual resistivity of the ferromagnetic part. The values of ρ_m^* are displayed in Table VII. The values are of about the same magnitude as the ones reported for Fe_3Si. The cusp-type resistivity behavior was theoretically investigated by Kataoka.[85] According to his predictions the cusp-type resistivity anomaly is an indicator for half-metallic ferromagnetism which is in perfect agreement with the prediction of the band-structure calculations shown above.

Besides the anomaly in magnetic-scattering resistivity, changes in the electronic structure at the phase transition may also give a direct raise to changes in the temperature dependence of the resistivity. The calculations of the resis-

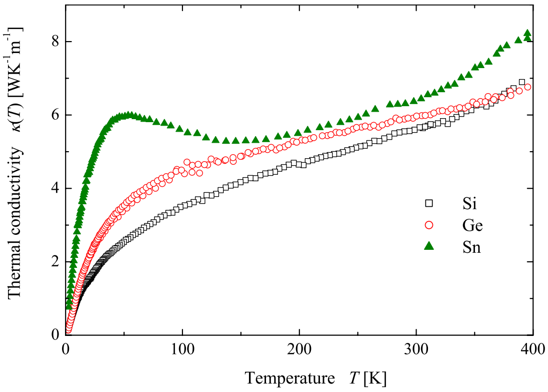

FIG. 20. (Color online) Measured thermal conductivity of Co_2TiZ compounds with Z=Si, Ge, Sn.

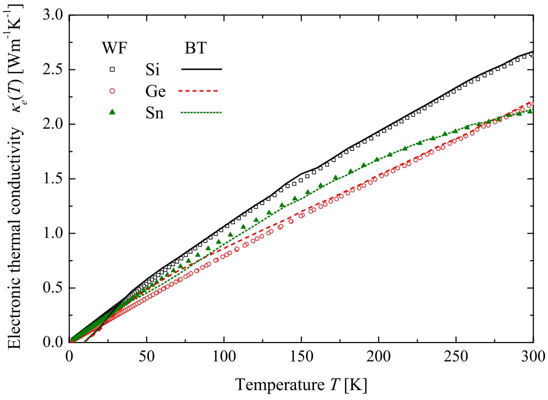

FIG. 21. (Color online) Temperature dependence of the electronic thermal conductivity of Co_2TiZ compounds with Z=Si, Ge Sn. Values obtained by the Wiedemann-Franz law using the measured resistivity are drawn as symbols (WF). Lines (BT) represent the calculated κ_0 values multiplied by a relaxation time τ [Eq. (8)].

tivity integrals (that is, resistivity ρ multiplied by the relaxation time τ) are displayed in Fig. 19.

In Fig. 19 the behavior of the resistivity of the compounds is shown for a temperature dependent, mixed magnetic state. For the mixing, the conductivity integrals (see Fig. 5) have been weighted according to the magnetization $m(T)$ shown in the inset of Fig. 19 for Co_2TiSi (for details see also Ref. 79). Displayed is the resistivity for a weighted mixture of a spin-polarized and a non-spin-polarized calculation. The weighting has been calculated according to a normalization of the magnetization at 5 K, which is assumed to be 100% at this temperature. It should be kept in mind that the resistivity integral respects only the temperature-dependent changes in the electronic structure in the vicinity of the Fermi energy. Whereas all other temperature effects are included in the relaxation time τ that will also change with temperature and includes all quasiparticle excitations (phonons, magnons, etc.) and all scattering-related effects. For low temperatures the ferromagnetic behavior dominates the resistivity integral and it is sharply declining at the Curie temperature. For temperatures above the Curie temperature, the resistivity integral behaves analogous to the non-spin-polarized calculation. A drop of about 25% of the resistivity integral is observed at the Curie temperature. This explains partially the experimentally observed change in the resistivity at the Curie temperatures very well, although the drop is not that sharp as expected. The peak is smeared out because of the temperature-dependent vanishing of the magnons, above the Curie temperature. Further the influence of different relaxation times is not negligible anymore (compare the τ values far below and far above T_C in Table:VII).

2. Thermal conductivity

For further evaluation of the compounds as possible magnetic and thermoelectric materials the thermal conductivity was measured in the range from 2 to 400 K. In Fig. 20 the thermal conductivities of the studied samples is displayed. For Co_2TiSi and Co_2TiGe the thermal conductivity is increasing with a T^3 law at low temperatures and then changing to a linear increase with T. Co_2TiSn follows the T^3 law too but reaches a maximum at about 50 K. From there the thermal conductivity decreases according to the T^{-1} law to the temperature of 140 K. Afterward the thermal conductivity increases linearly as is observed for the other compounds.

The peak indicates, that the Co_2TiSn sample is well ordered and has only few defects. The bigger or more disordered the unit cell becomes, the more the low-temperature peak is discriminated. The thermal conductivity may be separated into two parts by $\kappa = \kappa_e + \kappa_l$. κ_e is the electronic contribution and κ_l is the lattice contribution. Figure 21 displays the experimental and the calculated results of the electronic part of the thermal conductivity κ_e. The experimental results are derived from the resistivity using the Wiedemann-Franz law. The theoretical data are results of the calculation as described above. The electron of the minority channel were neglected due to their small contribution in this temperature range. The scattering factor has been determined by comparison of the experimental and calculated results of the resistivity. The agreement of the values is very good for all three compounds. From the calculation of $\kappa_e + \kappa_l$ one finds ratios of κ_e/κ_l of 1.03, 0.73, and 0.74 at 300 K for Co_2TiSi, Co_2TiGe, and Co_2TiSn. These ratios may need further optimization to reach a value of 0.5 which is proposed[86] to be the best ratio with respect to a high figure of merit. The temperature-dependent electronic part of the thermal conductivity is displayed in Fig. 21. The dotted lines represent the calculated values multiplied by the relaxation time τ.

In Fig. 22 the lattice thermal conductivity for Co_2TiZ (Z=Si, Ge, Sn) is shown. For all three compounds the thermal conductivity increases according to the T^3 law for low temperatures. For Co_2TiSi and Co_2TiGe the phononic part of the thermal conductivity stays constant above 100 K with 3.4 W m^{-1} K^{-1} and 3.8 W m^{-1} K^{-1}, respectively. For Co_2TiSn a pronounced peak is observed at about 40 K. This can be explained by a dominating phononic part of the thermal conductivity by boundary scattering, that is diminishing for higher temperatures, see Eq. (14). For temperatures above 250 K a small increase is observed. The increase is explained by a change in the duration of the measurement time leading to a small increase in the values. The increase in the total thermal conductivity is only related to the electronic contribution above 150 K.

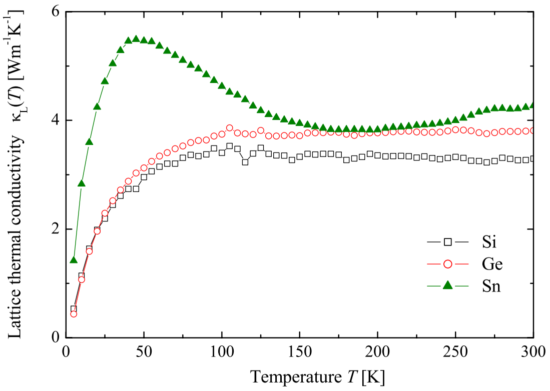

FIG. 22. (Color online) Lattice thermal conductivity of Co_2TiZ compounds with Z=Si, Ge, Sn.

3. Seebeck coefficient

Figure 23 shows the Seebeck coefficient that was measured for temperatures from 2 to 950 K. The values decrease with increasing temperature up to the Curie temperature and stay nearly constant at higher temperature. The mean values above T_C are −31, −35, or −51 μV K^{-1} for Co_2TiSi, Co_2TiGe, or Co_2TiSn, respectively. The maximum absolute values are rather large compared to the most elemental metals and are close to the Seebeck coefficient of elemental Co that exhibits about −30 to −45 μV K^{-1} at temperatures between 300 and 500 K.[87]

The Seebeck coefficient of all three investigated compounds is negative over the entire temperature range. For Co_2TiSn a negative increase in the Seebeck coefficient is observed at about 80 K. This is close to $T/\Theta_D \approx 0.2$ with Θ_D being the Debye temperature where the largest influence of a phonon drag is expected. This assumption is in agreement with the measurement of the thermal conductivity where a peak at low temperatures is observed.

As seen from Eq. (11) the Seebeck coefficient is, to a first approximation, independent of the relaxation time. It provides a sensitive test of the electronic structure for metals in the vicinity of the Fermi energy. From the calculations reported in Sec. IV A, the density of states is slightly increasing in the ferromagnetic case whereas it is decreasing in the non-spin-polarized case which leads to opposite signs for the Seebeck coefficient in comparison of both cases. The experimentally determined Seebeck coefficient is clearly negative at $T > 50$ K. This is not explained by the ferromagnetic electronic structure which is dominated by the majority electrons even if a mixing with the minority states is assumed at $T > 0$. For a better description the non-spin-polarized and the ferromagnetic calculations may be mixed as used before for a partial explanation of the anomalous resistivity.

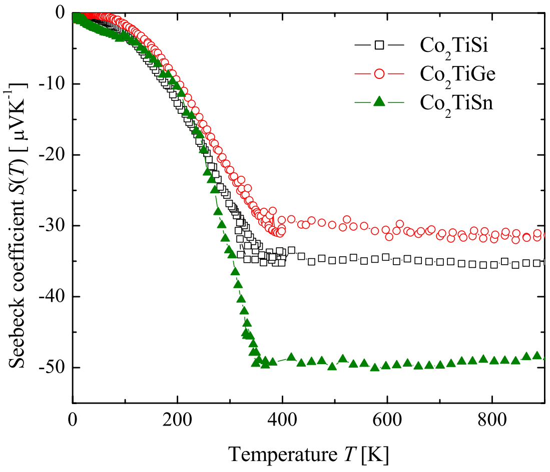

FIG. 23. (Color online) Measured Seebeck coefficient of Co_2TiZ compounds with Z=Si, Ge, Sn.

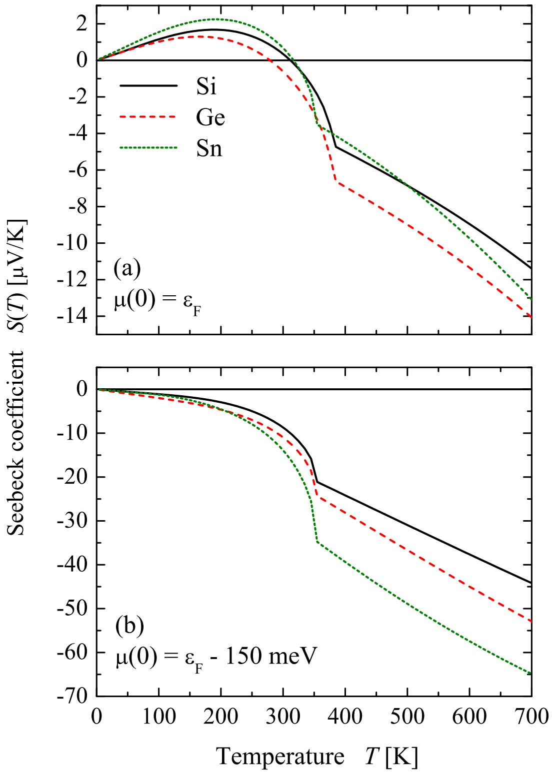

FIG. 24. (Color online) Calculated temperature dependence of the Seebeck coefficient for a mixture of ferromagnetic and non-spin-polarized states. (a) shows $S(T)$ calculated for the chemical potential at T=0 set to the Fermi energy. (b) shows $S(T)$ calculated for the chemical potential at T=0 shifted 150 meV below the calculated Fermi energy (compare Fig. 7). $S(T)$ was calculated using the same model for the magnetization as for the resistivity in Fig. 19.

In Fig. 24 the Seebeck coefficient is calculated in the temperature range from 5 to 700 K for the mixed ferromagnetic and non-spin-polarized electronic structure with weights according to a molecular-field approximation (see also Ref. 79). In the ferromagnetic low-temperature region the Seebeck coefficient is positive for all three compounds if the chemical potential at 0 K is set to the calculated Fermi energy [Fig. 24(a)]. It becomes negative already at temperatures below T_C and stays negative in the non-spin-polarized region. The values for the Seebeck coefficient are still too small, even if a total non-spin-polarized behavior is assumed far above T_C. The calculations demonstrate, nevertheless, how the Seebeck coefficient is strongly effected when the electronic structure is considerably changed while crossing the magnetic phase transition.

Larger Seebeck coefficients may be explained by additional scattering at grain boundaries or impurities inside of the sample, however, this will not change its sign. In Sec. II A, Fig. 7 it was demonstrated that already small changes in the chemical potential caused by imperfections of the sample are able to change the sign and magnitude of the Seebeck coefficient and therefore are able to explain the different sign observed in the calculations as well as the different magnitude. It is well known that the Seebeck coefficient is very sensitive to the state of the sample and already small changes in the electron density will change its behavior. Figure 24(b) shows the calculated result if the chemical potential at 0 K is shifted to 150 meV below the Fermi energy. Here, the calculated $S(T)$ stays negative over the entire temperature range and its shape is much closer to the experimental situation. The calculation does, however, not explain the constant Seebeck effect above T_C, even though the use of different shifts for the chemical potential of the different compounds may lead to an even better correspondence to the experiment.

The constant value of the Seebeck effect may better be interpreted by analyzing Eq. (9) in some more detail. Since S is constant, the product of σ^{-1} and ν has to be constant. The observed decrease in σ has to be exactly compensated by the influence of the relaxation time τ. A further consequence of the description by a partial or complete non-spin-polarized behavior is that the number of bands crossing the Fermi energy increases. Generally τ dependents on the character of the bands and therefore the conductivity integrals for electronic and thermal transport may be approximated by

$$\sigma/\tau = \frac{\Sigma \sigma_i \tau_i}{\Sigma \tau_i},$$

$$\nu/\tau = \frac{\Sigma \nu_i \tau_i}{\Sigma \tau_i}. \qquad (19)$$

Assuming that the τ_i depend only on the band index i but not on E or k the Seebeck coefficient depends on the relaxation times τ_i of the contributing bands,

$$S = \frac{\Sigma \nu_i \tau_i}{\Sigma \sigma_i \tau_i}. \qquad (20)$$

As mentioned in Sec. IV A only one band is crossing the Fermi energy in the half-metallic ferromagnetic ground state (t_{2g} majority band) and thus an influence of different relaxation times is not expected at low temperatures. The situation changes, however, in the non-spin-polarized case where several bands are crossing ϵ_F in all directions of high symmetry. This suggests that the constant Seebeck coefficient in the nonferromagnetic state above T_C is governed by effects of the relaxation time rather than by the pure influence of the band dispersion. At intermediate temperatures a rather complicated behavior is expected. Figure 25 shows the figure of merit for temperatures below the Curie temperature of the compounds. ZT was calculated according to Eq. (17) using the measured resistivity, thermal conductivity, and Seebeck coefficient as reported above.

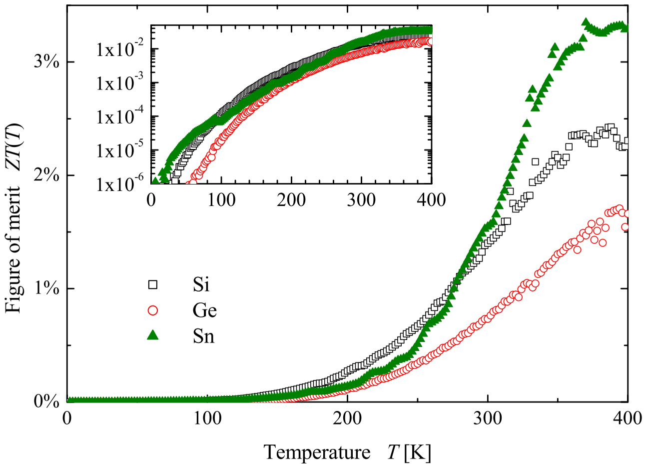

FIG. 25. (Color online) Measured figure of merit of Co_2TiZ compounds with Z=Si, Ge, Sn. The inset shows $ZT(T)$ on a logarithmic scale for better comparison of the low-temperature behavior.

V. SUMMARY AND CONCLUSION

The Co_2TiZ (Z=Si, Ge, Sn) Heusler compounds were investigated theoretically and experimentally with respect to electronic, magnetic, and thermoelectric properties. The main focus was on the influence of the main group element on the properties related to the electronic structure. Independent of the main group element, extraordinary anomalies were found for the transport properties that are caused by the peculiar electronic structure of the compounds.

Ab initio electronic- and vibrational-structure calculations on the basis of the FLAPW method were carried out. Spin-polarized calculations predict half-metallic ferromagnetism for all three compounds with an approximate energy gap in the minority states of 0.5–0.79 eV. The calculated magnetic moments are $2\mu_B$ with each Co atom carrying $1\mu_B$. The compounds were found to be completely itinerant. The electronic structure was calculated for non-spin-polarized and spin-polarized cases with a significant influence on the band structure. The electrical conductivities σ and the Seebeck coefficient S were calculated for the spin-polarized and the non-spin-polarized cases and comparisons with regard to the band structure were made. The figure of merit ZT_e was calculated using the electronic part of the thermal conductivity κ_e yielding considerably higher values for the nonpolarized case. It was shown that already small shifts of the chemical potential have a strong impact on the Seebeck coefficient. The transport properties are not only influenced by the electrons but also by the phonons. Therefore, the vibrational properties of the compounds were calculated. The phonon band width is largest for Co_2TiSi and decreases with higher atomic numbers at the Z position due to the increase in the mass of the main group element. The lattice specific heat $C_L(T)$ was calculated and the Debye temperatures Θ_D were determined. In all cases the continuous change in the properties with increasing atomic number of the main group element were demonstrated.

The compounds were synthesized by arc melting and consequent annealing. EDX spectroscopy revealed homogeneous sample compositions. The crystalline structure was investigated by XRD and it was found that the compounds exhibit the $L2_1$ structure with an increasing lattice parameter if going from Si to Sn. By temperature-dependent XRD measurements a linear-expansion coefficient ($\approx 5\times 10^{-6}$ K^{-1}) in the typical range for transition metals was found that is nearly independent of the composition. High-energy photoelectron spectroscopy was performed and the results confirmed the calculated electronic structure. The bulk-sensitive valence-band spectra agree well with the calculated density of states. The determined magnetic properties that are Curie temperature (about 380 K) and the magnetic moment ($2\mu_B$) are in good agreement with the theoretical predictions. In the resistivity measurements a metallic behavior was observed at low temperatures. The thermal conductivity κ was determined and separated into the electronic part κ_e and the phononic part κ_l using the Wiedemann-Franz law. From the electric-transport measurements the highest resistivity (3.5 $\mu\Omega$ m) and Seebeck coefficient -50 μV K^{-1} was found for Co_2TiSn for high temperatures. This compound exhibits also the highest figure of merit *ZT* with about 3% at 300 K. In some details, Co_2TiSn behaves slightly different from the Si- or Ge-containing compounds. This is explained by the larger lattice parameter and heavier mass of Sn. The larger a influences the electronic structure and the mass the vibrational properties that enter both together all transport properties.

Most remarkable is the temperature dependence of the transport properties, especially of the resistivity and the Seebeck effect. The compounds exhibit a pronounced cusp-type anomaly of the resistivity at the Curie temperature. The cusp is associated to the ferromagnetic to paramagnetic phase transition. For $T \geq T_C$ a negative temperature coefficient is observed and explained by the magnetic-scattering resistivity. The highest value for the magnetic-scattering resistivity ρ_m^* was found for the Sn-containing compound. The resistivity becomes nearly constant for temperatures well above T_C. The measurement of the Seebeck coefficient revealed also an anomalous behavior. Below T_C its temperature dependence follows the temperature dependence of the magnetization rather than a pure temperature dependent occupation of holes and excited electrons close to the Fermi energy. Most interesting it becomes constant for $T \geq T_C$ for all three compounds. This points on distinct changes in the electronic structure when crossing the magnetic phase transition. The results are explained by a shift of the chemical potential and the inclusion of both the spin-polarized and the nonpolarized electronic structure.

ACKNOWLEDGMENTS

This work is financially supported by Stiftung Rheinland-Pfalz für Innovation, the Deutsche Forschungsgemeinschaft DFG (projects P 1 and P 7 in research unit FOR 559), and DAAD (D06/33952). The authors thank the staff of the LNLS (Campinas) for support as well as Fabiano Bernardi (Porto Allegre), Fabio Furlan Ferreira, and Gustavo Azevedo (LNLS, Campinas) for help with the XRD and EXAFS experiments. Further support of this work was provided by the Brazilian Synchrotron Light Laboratory (LNLS) under proposals D10B-XPD-6689 and D04B-XAFS1-6699. The HAXPES measurements were performed under the approval of NIMS (Proposal No. 2008A4905). The experiments at BL15XU of SPring-8 were partly supported by the Nanotechnology Network Project, the Ministry of Education, Culture, Sports, Science and Technology (MEXT), Japan. The authors are grateful to HiSOR, Hiroshima University and JAEA/SPring-8 for the development of HAXPES at BL-15XU.

---

*felser@uni-mainz.de

[1] J. Kübler, A. R. Williams, and C. B. Sommers, Phys. Rev. B **28**, 1745 (1983).

[2] S. Ishida, J. Phys. Soc. Jpn. **53**, 2718 (1984).

[3] S. Ishida, S. Fujii, S. Kashiwagi, and S. Asano, J. Phys. Soc. Jpn. **64**, 2152 (1995).

[4] I. Galanakis, P. H. Dederichs, and N. Papanikolaou, Phys. Rev. B **66**, 174429 (2002).

[5] H. C. Kandpal, G. H. Fecher, and C. Felser, J. Phys. D; Appl. Phys. **40**, 1507 (2007).

[6] R. A. de Groot, F. M. Mueller, P. G. van Engen, and K. H. J. Buschow, Phys. Rev. Lett. **50**, 2024 (1983).

[7] B. Sales, B. Chakoumakos, D. Mandrus, and J. Sharp, J. Solid State Chem. **146**, 528 (1999).

[8] F. Rosi, Solid-State Electron. **11**, 833 (1968).

[9] T. C. Harman, P. Taylor, M. Walsh, and B. LaForge, Science **297**, 2229 (2002).

[10] S. Ogut and K. M. Rabe, Phys. Rev. B **51**, 10443 (1995).

[11] S. Sakurada and N. Shutoh, Appl. Phys. Lett. **86**, 082105 (2005).

[12] Y. Nishino, H. Kato, M. Kato, and U. Mizutani, Phys. Rev. B **63**, 233303 (2001).

[13] C. S. Lue, C. F. Chen, J. Y. Lin, Y. T. Yu, and Y. K. Kuo, Phys. Rev. B **75**, 064204 (2007).

[14] D. Rowe, *CRC Handbook of Thermoelectrics* (CRC, Boca Raton, 1995).

[15] P. Blaha, K. Schwarz, P. Sorantin, and S. Tricky, Comput. Phys. Commun. **59**, 399 (1990).

[16] P. Blaha, K. Schwarz, G. K. H. Madsen, D. Kvasnicka, and J. Luitz, *WIEN2k, An Augmented Plane Wave Plus Local Orbitals Program for Calculating Crystal Properties*, edited by K. Schwarz (Wien Technical University, Austria, 2001).

[17] J. P. Perdew, K. Burke, and M. Ernzerhof, Phys. Rev. Lett. **77**, 3865 (1996).

[18] G. K. H. Madsen and D. J. Singh, Comput. Phys. Commun. **175**, 67 (2006).

[19] J. M. Ziman, *Electrons and Phonons* (Oxford University Press, Oxford, New York, 1960).

[20] U. Mizutani, *Electron Theory of Metals* (Cambridge University Press, Cambridge, 2001).

[21] W. Jones and N. H. March, *Theoretical Solid State Physics* (Dover, New York, 1985), Vol. II.

[22] W. W. Schulz, P. B. Allen, and N. Trivedi, Phys. Rev. B **45**, 10886 (1992).

[23] K. Parlinski, *Software* PHONON (2006).

[24] P. Bruesch, *Phonons: Theory and Experiments* (Springer-Verlag, Berlin, 1982).

[25] F. F. Ferreira, E. Granado, C. J. Wilson, S. W. Kycia, D. Bruno, and D. J. Roosevelt, J. Synchrotron Radiat. **13**, 46 (2006).

[26] E. Müller, C. Stiewe, D. Rowe, and S. Williams, *Thermoelectrics Handbook Macro To Nano* (CRC, Boca Raton, 2006).

[27] Q. Design, *Physical Property Measurement System Thermal Transport Option User's Manual* (Quantum Design, San Diego, 2002).

[28] M. C. Hickey, A. Husmann, S. Holmes, and G. Jones, J. Phys.: Condens. Matter **18**, 2897 (2006).

[29] S. Ishida, S. Akazawa, Y. Kubo, and J. Ishida, J. Phys. F: Met. Phys. **12**, 1111 (1982).

[30] S. C. Lee, T. D. Lee, P. Blaha, and K. Schwarz, J. Appl. Phys. **97**, 10c307 (2005).

[31] P. Klaer, M. Kallmayer, C. G. R. Blum, T. Graf, B. Balke, J. Barth, G. H. Fecher, C. Felser, and H. J. Elmers, Phys. Rev. B **80**, 144405 (2009).

[32] P. Weinberger, *Electron Scattering for Ordered and Disordered Matter* (Clarendon, Oxford, 1990).

[33] G. E. Bacon and J. S. Plant, J. Phys. F: Met. Phys. **1**, 524 (1971).

[34] B. Ravel, M. P. Raphael, V. G. Harris, R. Ramesh, and V. Saraf, Appl. Phys. Lett. **81**, 2812 (2002).

[35] K. Buschow, P. van Engen, and R. Jongebreur, J. Magn. Magn. Mater. **38**, 1 (1983).

[36] P. J. Webster and K. Ziebeck, J. Phys. Chem. Solids **34**, 1647 (1973).

[37] P. van Engen, K. Buschow, and M. Erman, J. Magn. Magn. Mater. **30**, 374 (1983).

[38] J. Zhao, A. V. Bragas, R. Merlin, and D. J. Lockwood, Phys. Rev. B **73**, 184434 (2006).

[39] M. Kido, H. Ido, and G. Kido, J. Magn. Magn. Mater. **104-107**, 705 (1992).

[40] A. W. Carbonari, W. J. Pendl, R. N. Attili, and R. N. Saxena, Hyperfine Interact. **80**, 971 (1993).

[41] J. Pierre, R. Skolozdra, and Y. V. Stadnyk, J. Magn. Magn. Mater. **128**, 93 (1993).

[42] A. Yamasaki, S. Imada, R. Arai, H. Utsunomiya, S. Suga, T. Muro, Y. Saitoh, T. Kanomata, and S. Ishida, Phys. Rev. B **65**, 104410 (2002).

[43] H. Kandpal, V. Ksenofontov, M. Wojcik, R. Seshadri, and C. Felser, J. Phys. D **40**, 1587 (2007).

[44] M. Kawakami, Hyperfine Interact. **51**, 993 (1989).

[45] E. I. Gladyshevskii, Powder Metallurgy and Metal Ceramics, Poroshkovaya Metallurgiya (Kiev) **1**, 262 (1962).

[46] S. Plogmann, T. Schlathölter, J. Braun, M. Newmann, Y. M. Yarmoshenko, M. Yablonskikh, E. I. Shreder, E. Z. Kurmaev, A. Wrona, and A. Slebarski, Phys. Rev. B **60**, 6428 (1999).

[47] H. Ido, J. Magn. Magn. Mater. **54-57**, 937 (1986).

[48] R. Sobzcak, J. Phys. (Paris), Colloq. **49**, 141 (1988).

[49] M. P. Raphael, B. Ravel, Q. Huang, M. A. Willard, S. F. Cheng, B. N. Das, R. M. Stroud, K. M. Bussmann, J. H. Claassen, and V. G. Harris, Phys. Rev. B **66**, 104429 (2002).

[50] L. Ritchie, G. Xiao, Y. Ji, T. Y. Chen, C. L. Chien, M. Zhang, J. Chen, Z. Liu, G. Wu, and X. X. Zhang, Phys. Rev. B **68**, 104430 (2003).

[51] L. Castelliz, Monatsch. Chem. **84**, 765 (1953).

[52] A. Szytula, A. Kolodziejczyk, H. Rzany, J. Todorovic, and A. Wanic, Phys. Status Solidi A **11**, 57 (1972).

[53] E. Uhl, Solid State Commun. **53**, 395 (1985).

[54] W. Zhang, N. Jiko, K. Mibu, and K. Yoshimura, J. Phys.: Condens. Matter **17**, 6653 (2005).

[55] V. Niculescu, J. I. Budnick, W. A. Hines, K. Raj, S. Pickart, and S. Skalski, Phys. Rev. B **19**, 452 (1979).

[56] S. Wurmehl, G. H. Fecher, V. Ksenofontov, C. Felser, and H.-J. Lin, Appl. Phys. Lett. **88**, 032503 (2006).

[57] S. Wurmehl, G. H. Fecher, V. Ksenofontov, F. Casper, U. Stumm, C. Felser, and H.-J. Lin, J. Appl. Phys. **99**, 08J103 (2006).

[58] J. G. Booth and R. G. Pritchard, J. Phys. F: Met. Phys. **5**, 347 (1975).

[59] K. Ooiwa, J. Phys. Soc. Jpn. **54**, 1581 (1985).

[60] T. Sasaki, T. Kanomata, T. Narita, H. Nishihara, R. Note, H. Yoshida, and T. Kaneko, J. Alloys Compd. **317-318**, 406 (2001).

[61] K. H. J. Buschow and P. G. van Engen, J. Magn. Magn. Mater. **25**, 90 (1981).

[62] A. W. Carbonari, R. N. Saxena, W. Pendl, Jr., J. Mestnik Filho, R. N. Attili, M. Olzon-Dionysio, and S. D. de Souza, J. Magn. Magn. Mater. **163**, 313 (1996).

[63] K. Kobayashi, R. Y. Umetsu, A. Fujita, K. Oikawa, R. Kainuma, K. Fukamichi, and K. Ishida, J. Alloys Compd. **399**, 60 (2005).

[64] R. Y. Umetsu, K. Kobayashi, A. Fujita, K. Oikawa, R. Kainuma, K. Ishida, N. Endo, K. Fukamichi, and A. Sakuma, Phys. Rev. B **72**, 214412 (2005).

[65] S. Wurmehl, G. H. Fecher, and C. Felser, Z. Anorg. Allg. Chem. **61b**, 749 (2006).

[66] H. J. Elmers, S. Wurmehl, G. H. Fecher, G. Jakob, C. Felser, and G. Schönhense, Appl. Phys. A: Mater. Sci. Process. **79**, 557 (2004).

[67] M. Zhang, E. Brück, F. R. de Boer, Z. Li, and G. Wu, J. Phys. D: Appl. Phys. **37**, 2049 (2004).

[68] P. F. Schmidt, *Praxis der Rasterelektronenmikroskopie und Mikrobereichsanalyse* (ExpertVerlag, Renningen, Germany, 1994).

[69] S. Ouardi, A. Gloskovskii, B. Balke, C. A. Jenkins, J. Barth, G. H. Fecher, C. Felser, M. Gorgoi, M. Mertin, F. Schäfers, E. Ikenaga, K. Yang, K. Kobayashi, T. Kubota, M. Oogane, and Y. Ando, J. Phys. D: Appl. Phys. **42**, 084011 (2009).

[70] G. H. Fecher, H. C. Kandpal, S. Wurmehl, and C. Felser, J. Appl. Phys. **99**, 08J106 (2006).

[71] J. Kübler, J. Phys.: Condens. Matter **18**, 9795 (2006).

[72] J. Kübler, G. H. Fecher, and C. Felser, Phys. Rev. B **76**, 024414 (2007).

[73] S. Majumdar, M. K. Chattopadhyay, V. K. Sharma, K. J. S. Sokhey, S. B. Roy, and P. Chaddah, Phys. Rev. B **72**, 012417 (2005).

[74] T. J. Scheidemantel, C. Ambrosch-Draxl, T. Thonhauser, J. V. Badding, and J. O. Sofo, Phys. Rev. B **68**, 125210 (2003).

[75] L. Lykke, B. B. Iversen, and G. K. H. Madsen, Phys. Rev. B **73**, 195121 (2006).

[76] N. W. Ashcroft and N. D. Mermin, *Solid State Physics* (Saunders, Orlando, Florida, 1976).

[77] F. C. Zumsteg and R. D. Parks, Phys. Rev. Lett. **24**, 520 (1970).

[78] L. W. Shacklette, Phys. Rev. B **9**, 3789 (1974).

[79] T. Graf, G. H. Fecher, J. Barth, J. Winterlik, and C. Felser, J. Phys. D: Appl. Phys. **42**, 084003 (2009).

[80] H. E. Nigh, S. Legvold, and F. H. Spedding, Phys. Rev. **132**, 1092 (1963).

[81] W. J. Nellis and S. Legvold, Phys. Rev. **180**, 581 (1969).

[82] M. P. Kawatra, S. Skalski, J. A. Mydosh, and J. L. Budnick, Phys. Rev. Lett. **23**, 83 (1969).

[83] Y. Nishino, S. Y. Inoue, S. Asano, and N. Kawamiya, Phys. Rev. B **48**, 13607 (1993).

[84] A. Hamzic, R. Asomoza, and I. A. Campbell, J. Phys. F: Met. Phys. **11**, 1441 (1981).

[85] M. Kataoka, Phys. Rev. B **63**, 134435 (2001).

[86] C. M. Bhandari, *CRC Handbook of Thermoelectrics* (CRC, Boca Raton, 1995).

[87] J. Nyström, *Zahlenwerte und Funktionen, II. Band* (Springer-Verlag, Heidelberg, Germany, 1959).